4. Experimental section

4.1. General methods and materials

All reactions were carried out under an atmosphere of argon. ^{1}H NMR spectra were obtained at 300 MHz on a Varian MERCURY 300 spectrometer with tetramethylsilane (TMS) as an internal standard in $CDCl_3$. ^{13}C NMR spectra were obtained at 75.45 MHz on a Varian MERCURY 300 spectrometer with $CDCl_3$ as an internal standard (δ 77.0) in $CDCl_3$. Mass spectra were recorded on Voyager System 4327 (Applied Biosystem). Analytical TLC was performed on Merck Kieselgel 60-F254 plates. Melting curves of nucleic acid duplexes were recorded on a UV-1650PC UV–visible spectrophotometer (Shimadzu). CD spectra were measured on a J-725 spectropolarimeter (JASCO). Fluorescence anisotropies were recorded on a FP-6500 spectrofluorometer (JASCO). Silica gel column chromatography was carried out using Silica gel 60 N (63–210 μm or 40–50 μm). Reversed phase HPLC was carried out using a μBondasphere 5-μm C4 or C18, 100 Å, 4 mm × 150 mm (Waters) with a gradient of 0–100% acetonitrile in water at 25 °C at a rate of 0.5 mL/min and acetonitrile and water is buffered by TFA (trifluoroacetic acid) with 0.05% v/v. Organic solvents were purified and dried by the appropriate procedure. RNA oligomers were purchased from Hokkaido System Science Co., Ltd and Japan Bio Services Co., Ltd. The yields of compounds were calculated from their dry weights except for **14**, **18** and **21**. The yields of **14** and **18** were estimated from absorbance compared with that of corresponding vitamin E derivatives. The yield of **21** was estimated from absorbance of $MMTr^+$ generated by deprotection.

4.1.1. Conditions for the UV melting analyses

Absorbance versus temperature profile measurements were carried out with eight-sample cell changer, in quarts cells of 1 cm pathlength. The variation of the difference of UV absorbance at between 260 nm and 320 nm with temperature was monitored. The temperature was scanned between 0 °C and 95 °C, and the rate of temperature increase was 0.2 °C/min. Oligonucleotides were annealed after addition of amino sugars. The samples containing oligonucleotides and amino sugars were first rapidly heated to 95 °C, left for 20 min, and then allowed to cool slowly to room temperature. These samples were furthermore cooled to 0 °C and left for 1 h, and then the dissociation was recorded by heating to 95 °C at rate of 0.2 °C/min.

4.1.2. Conditions for the CD spectrometry

All of the CD spectra were recorded at 25 °C. The following instrument settings were used: resolution, 0.1 nm; sensitivity, 10 mdeg; response, 4 s; speed, 10 nm/min; accumulation, 6.

4.1.3. Conditions for the fluorescence anisotropy measurement

The all titrations were measured at 20 °C. The following instrument settings were used: Ex/Em = 490 nm/520 nm; response, 2 s; Band width (Ex), 5 nm; Band width (Em), 5 nm; PMT voltage, 450 V; No. of cycle, 4;

4.2. Phenyl 2,6-dideoxy-2,6-diphthalimimde-1-thio-β-D-galactopyranoside (2)

Compound **1** (6.74 g, 16.8 mmol), triphenylphosphine (8.81 g, 33.6 mmol, 2.0 equiv), and phthalimide (4.94 g, 33.6 mmol, 2.0 equiv) were dissolved in dry tetrahydrofurane (168 mL) and cooled to 0 °C. To this mixture, diisopropyl azodicarboxylate (6.5 mL, 33.6 mmol, 2.0 equiv) was added dropwise over 20 min. After 40 min, further diisopropyl azodicarboxylate (3.0 mL) was added. After 30 min, methanol (20 mL) was added to the mixture and the solvent was evaporated. The crude product was recrystallized from methanol (50 mL) and then from ethyl acetate-hexane (1:5, v/v, 180 mL), and **2** was obtained as a colorless solid (6.28 g, 11.8 mmol, 71%).

^{1}H NMR ($CDCl_3$) δ 7.91–7.69 (m, 8H, N*Phth*), 7.39–7.34 (m, 2H, S*Ph*), 7.20–7.10 (m, 3H, S*Ph*), 5.59 (d, J = 10.2, 1H, H-1), 4.48–4.32 (m, 2H, H-2, H-3), 4.19–4.12 (m, 1H), 4.00–3.83 (m, 3H, 4-H), 3.62 (d, J = 5.1, 1H, 4-OH), 2.68 (d, J = 10.8, 1H, 3-OH).

^{13}C NMR ($CDCl_3$) δ 168.7, 134.6, 134.1, 132.7, 132.0, 131.8, 131.7, 131.6, 128.8, 127.9, 123.8, 123.7, 123.3, 84.0, 75.1, 68.6, 67.8, 53.1, 37.3.

MALDI-TOF MS: m/z calcd for $C_{36}H_{30}N_2NaO_8S$ $[M+Na]^+$: 553.10 Found: 553.11.

4.3. Phenyl 2,6-dideoxy-2,6-diphthalimimde-3-*O*-*p*-methoxybenzyl-1-thio-β-D-galactopyranoside (3)

Compound **2** (6.28 g, 11.8 mmol) was coevaporated with dry toluene (10 mL × 4) and dissolved in dry toluene (200 mL). Dibutyltin oxide (3.25 g, 13.0 mmol, 1.1 equiv) was added to the solution and it was refluxed for 12.5 h. Tetrabutylammonium iodide (4.81 g, 13.0 mmol, 1.1 equiv) and *p*-methoxybenzyl chloride (1.55 mL, 13.0 mmol, 1.1 equiv) was added. After 5.5 h, the mixture was cooled to rt and concentrated to dryness. The crude product was purified by silica gel column chromatography (dichloromethane (1.5% methanol)). The purified product was dissolved in toluene–dichloromethane–ethyl acetate (8:1:1, v/v/v, 500 mL) and washed with water (200 mL × 3). The product was further purified by silica gel column chromatography (dichloromethane (1.5% methanol)) and **3** was obtained as a colorless foam (7.35 g, 11.0 mmol, 93%).

^{1}H NMR ($CDCl_3$) δ 7.88–7.63 (m, 8H, N*Phth*), 7.23–7.16 (m, 2H, Ar), 6.97–6.82 (m, 5H, Ar), 6.45 (d, J = 8.7, 2H, Ar), 5.36 (d, J = 8.7, 1H, H-1), 4.57–4.50 (m, 2H, ArCH_2-a, H-2), 4.43–4.36 (m, 1H, H-5), 4.27–4.21 (m, 2H, ArCH_2-b, H-3), 4.08 (s, 1H, 4-H), 4.01–3.97 (m, 1H, H-6a), 3.82–3.76 (m, 1H, H-6b), 3.65 (s, 3H, CH_3OPh), 2.74 (d, J = 0.9, 1H, 4-OH).

^{13}C NMR ($CDCl_3$) δ 168.1, 167.9, 167.3, 159.1, 134.0, 133.9, 133.8, 132.9, 131.9, 131.8, 131.6, 131.5, 129.6, 129.0, 128.3, 127.6, 123.4, 123.1, 113.6, 83.7, 75.0, 74.9, 71.0, 66.0, 54.9, 50.7, 38.9.

MALDI-TOF MS: m/z calcd for $C_{36}H_{30}N_2NaO_8S$ $[M+Na]^+$: 673.16 Found: 673.08.

4.4. Phenyl 4-*O*-chloroacetyl-2,6-dideoxy-2,6-diphthalimimde-3-*O*-*p*-methoxybenzyl-1-thio-β-D-galactopyranoside (4)

Compound **3** (7.35 g, 11.0 mmol) was dissolved in a mixed solvent of pyridine-dichloromethane (1:20, v/v, 126 mL) and cooled to 0 °C. To the solution was added chloroacetyl chloride (1.75 mL, 22.0 mmol, 2.0 equiv). After 25 min, the solution was diluted with toluene and the solvent was evaporated. The crude product was purified by silica gel column chromatography (chloroform (0.5% ethanol)) and **4** was obtained as a colorless foam (7.39 g, 10.2 mmol, 93%).

^{1}H NMR($CDCl_3$) δ 7.88–7.60 (m, 8H, N*Phth*), 7.29–7.26 (m, 2H, Ar), 7.07–6.94 (m, 3H, Ar), 6.83 (d, J = 7.2, 2H), 6.38 (d, J = 8.4, 2H), 5.54 (d, J = 2.7, 1H, 4-H), 5.46 (d, J = 10.5, 1H, H-1), 4.45–4.23 (m, 6H, ClAc, ArCH_2-a, H-2, H-3, H-5), 4.12–3.98 (m, 2H, ArCH_2-b, H-6a), 3.88–3.81 (m, 1H, H-6b), 3.64 (s, 3H, CH_3OPh).

^{13}C NMR ($CDCl_3$) δ 167.9, 167.6, 167.4, 167.2, 159.1, 134.2, 133.9, 133.8, 133.0, 131.7, 131.5, 131.4, 129.8, 128.9, 128.5, 127.9, 123.5, 123.4, 123.1, 113.5, 83.9, 73.4, 72.8, 70.9, 68.0, 54.9, 51.1, 41.1, 38.1.

MALDI-TOF MS: *m/z* calcd for $C_{38}H_{31}ClN_2NaO_9S$ $[M+Na]^+$: 749.13 Found: 749.12.

4.5. Compound 5

Compound **4** (0.1452 g, 200 μmol) was coevaporated with dry toluene (2 mL × 4). *N*-Iodosuccinimide (0.1127 g, 500 μmol, 2.5 equiv) and 3-bromo-1-propanol (36 μL, 400 μmol, 2.0 equiv) were added and the mixture was dissolved in dichloromethane (1.0 mL). The solution was cooled and then 0.2% trifluoromethanesulfonic acid in diethyl ether (1.0 mL) was added. After stirring for 20 min, a saturated aqueous solution of $NaHCO_3$ (1 mL) was added and the mixture was warmed to rt. The solution was diluted with chloroform (30 mL), washed with a saturated aqueous solution of $NaHCO_3$ (30 mL) and 10% $Na_2S_2O_3$aq (30 mL). The organic layer was dried over Na_2SO_4, filtered, and concentrated. After the crude product was cooled to 0 °C, 7.5 mM sodium methoxide solution in methanol (10 mL) and dichloromethane (5 mL) was added to the mixture. After 12.5 h, Dowex 50 W × 8 (2 g) was added, and stirred for 30 min and the Dowex resin was removed by filtration. The crude product was purified by silica gel column chromatography (ethyl acetate–toluene (1:4, v/v)) to afford the pure β-glycoside **5** as a colorless oil (0.1156 g, 170 μmol, 85%).

^{1}H NMR ($CDCl_3$) δ 7.91–7.65 (m, 8H, N*Phth*), 6.95 (d, *J* = 8.7, 2H, Ar), 6.46 (d, *J* = 8.4, 2H, Ar), 5.04 (d, *J* = 8.4, 1H, H-1), 4.54 (d, *J* = 12.6, 1H), 4.48–4.41 (m, 1H), 4.32–4.22 (m, 3H), 4.01–3.92 (m, 3H), 3.73–3.65 (m, 4H), 3.48–3.40 (m, 1H), 3.18–3.14 (m, 1H), 2.83 (s, 1H), 1.95–1.74 (m, 2H).

^{13}C NMR ($CDCl_3$) δ 168.2, 167.7, 159.0, 134.1, 133.8, 133.7, 131.8, 131.5, 129.4, 129.1, 123.4, 123.3, 122.9, 113.4, 98.4, 74.3, 71.5, 71.1, 66.5, 65.6, 54.9, 52.0, 38.5, 32.1, 30.2.

4.6. Compound 6

A mixture of **5** (50.4 mg, 71 μmol) and **4** (77.6 mg, 106 μmol, 1.5 equiv) was coevaporatated with dry toluene (2 mL × 4). *N*-Iodosuccinimide (59.9 mg, 265 μmol, 3.75 equiv) was added and the mixture was dissolved in dichloromethane (0.5 mL). The solution was cooled, and then 0.04% trifluoromethanesulfonic acid in diethyl ether (1.5 mL) was added to the solution. After 1.5 h, a saturated aqueous solution of $NaHCO_3$ (1 mL) was added and the mixture was warmed to rt. The solution was diluted with chloroform (30 mL), washed with a saturated aqueous solution of $NaHCO_3$ (30 mL) and 10% $Na_2S_2O_3$aq (30 mL). The organic layer was dried over Na_2SO_4, filtered, and concentrated. After the crude product was cooled to 0 °C, 7.5 mM sodium methoxide solution in methanol (10 mL) and dichloromethane (5 mL) was added to the mixture. After 13 h, Dowex 50 W × 8 (1 g) was added, stirred for 30 min and the Dowex resin was removed by filtration. The crude product was purified by silica gel column chromatography (ethyl acetate–toluene (7:13, v/v)) to afford the pure β-glycoside **6** as a colorless oil (68.7 mg, 56.3 μmol, 79%).

^{1}H NMR ($CDCl_3$) δ 8.10 (d, *J* = 7.8, 1H, Ar), 7.88–7.00 (m, 17H, Ar),.6.51–6.17 (m, 6H, Ar), 5.24 (d, *J* = 8.1, 1H, H-1), 4.74 (d, *J* = 8.4, H-1), 4.68–4.58 (m, 2H), 4.47–4.25 (m, 4H), 4.15–3.45 (m, 18H), 3.33–3.25 (m, 1H), 3.11–3.06 (m, 2H), 2.84 (d, *J* = 3.0, 1H), 1.87–1.67 (m, 2H).

^{13}C NMR ($CDCl_3$) δ 168.8, 168.1, 168.0, 167.8, 167.4, 166.1, 159.1, 158.6, 133.9, 133.8, 133.3, 133.2, 132.9, 132.7, 132.2, 131.8, 131.6, 131.4, 129.5, 129.3, 124.5, 123.5, 123.3, 123.2, 122.7, 122.5, 122.0, 113.6, 113.4, 113.1, 99.8, 97.7, 75.1, 74.4, 73.8, 72.1, 71.6, 71.0, 66.2, 65.4, 55.0, 54.8, 52.0, 51.4, 40.1, 39.4, 32.3, 30.6.

MALDI-TOF MS: *m/z* calcd for $C_{93}H_{79}BrN_6NaO_{25}$ $[M+Na]^+$: 1241.26 Found: 1241.26.

4.7. Compound 7

The same procedure for the synthesis of **6** was applied to that of **7**, except for using **6** (0.0942 g, 77 μmol) and **4** (0.1056 g, 146 μmol, 1.9 equiv) as starting materials, and ethyl acetate–toluene (9:11, v/v) as eluting solvent in silica gel column chromatography. Compound **7** was obtained as a colorless oil (0.1044 mg, 59 μmol, 77%).

^{1}H NMR ($CDCl_3$) δ 8.35 (d, *J* = 7.2, 1H, Ar), 7.91–7.05 (m, 27H, Ar), 6.52–6.07 (m, 8H, Ar), 5.24 (d, *J* = 8.7, 1H, H-1), 4.94 (d, *J* = 7.8, 1H, H-1), 4.76–4.51 (m, 4H), 4.37–4.00 (m, 10H), 3.93–3.43 (m, 21H), 3.31–3.08 (m, 4H), 1.95–1.73 (m, 2H).

^{13}C NMR ($CDCl_3$) δ 169.2, 168.4, 168.1, 168.0, 167.9, 167.6, 167.3, 166.1, 165.8, 159.0, 158.5, 158.4, 133.9, 133.7, 133.6, 133.3, 133.1, 133.0, 132.8, 132.4, 132.2, 132.0, 131.8, 131.6, 131.3, 129.7, 129.6, 129.4, 129.1, 129.1, 125.2, 123.8, 123.3, 123.2, 123.1, 122.6, 122.3, 122.0, 121.7, 113.5, 113.0, 112.9, 99.6, 99.5, 97.5, 75.1, 74.3, 74.0, 73.8, 72.8, 71.7, 71.6, 71.0, 70.8, 70.6, 66.4, 65.3, 55.0, 54.8, 54.7, 52.1, 51.8, 51.3, 40.5, 40.4, 39.4, 32.4, 30.8.

MALDI-TOF MS: *m/z* calcd for $C_{93}H_{79}BrN_6NaO_{25}$ $[M+Na]^+$: 1781.42 Found: 1781.39.

4.8. Compound 8

Compound **7** (21.9 mg, 12.5 μmol) was dissolved in dichloromethane (5 mL) and cooled to 0 °C. To the solution, 20% trifluoroacetic acid in dichloromethane (5 mL) was added and stirred for 2 h. The reaction was quenched by addition of a saturated aqueous solution of $NaHCO_3$ (5 mL) and diluted with dichloromethane (60 mL). The solution was washed with a saturated aqueous solution of $NaHCO_3$ (100 mL) and the aqueous layer was back extracted with dichloromethane (20 mL × 3). The organic layer was dried over Na_2SO_4, filtered and concentrated. The crude product was purified by silica gel column chromatography (dichloromethane (3% methanol)) and **8** was obtained as a colorless oil (12.4 mg, 8.9 μmol, 71%).

^{1}H NMR ($CDCl_3$) δ 8.03–7.60 (24H, N*Phth*), 5.69 (d, *J* = 8.1, 1H, H-1), 5.46 (d, *J* = 7.8, 1H, H-1), 4.81 (d, *J* = 8.1, 1H, H-1), 4.62–4.56 (m, 1H), 4.34–3.59 (m, 18H), 3.51–3.44 (m, 1H), 3.25–3.17 (m, 2H), 3.04–2.93 (m, 4H), 1.95–1.73 (m, 2H).

^{13}C NMR ($CDCl_3$) δ 168.5, 168.2, 167.9, 134.4, 133.9, 133.7, 132.2, 131.9, 131.7, 131.6, 124.1, 123.8, 123.5, 123.1, 99.3, 99.1, 98.5, 75.4, 75.3, 72.6, 72.4, 72.3, 71.2, 69.6, 68.9, 68.5, 66.7, 54.4, 54.2, 53.6, 39.8, 37.6, 31.9, 30.3.

MALDI-TOF MS: *m/z* calcd for $C_{69}H_{55}BrN_6NaO_{22}$ $[M+Na]^+$: 1421.24 Found: 1420.91.

4.9. Compound 11

α-Tocopherol **10** (0.2495 g, 0.58 mmol) was dissolved in dry *N*,*N*-dimethylformamide (6 mL). To the solution, sodium hydride (60% purity, 91.6 mg, 2.3 mmol, 4 equiv) and propargyl bromide (200 μL, 2.3 mmol, 4 equiv) were added. After 2 h, methanol was added and the mixture was concentrated to dryness. The mixture was dissolved in dichloromethane (50 mL) and washed with water (30 mL × 2). The crude product was purified by silica gel column chromatography (dichloromethane-hexane (1:9, v/v)) to give **11** as a pale yellow oil (0.2229 g, 0.474 mmol, 82%).

^{1}H NMR ($CDCl_3$) δ 4.36 (d, *s* = 2.7, 2H, HC≡CCH_2O), 2.57 (t, *J* = 6.6, 2H, ArCH_2), 2.48 (d, *J* = 2.1, 1H, *H*C≡C), 2.20–2.08 (s × 3, 9H, ArCH_3), 1.81–0.83 (m, 38H).

^{13}C NMR ($CDCl_3$) δ 127.9, 126.0, 122.9, 117.5, 74.9, 74.5, 60.5, 40.0, 39.3, 37.4, 37.3, 32.8, 32.7, 31.2, 28.0, 24.8, 24.4, 23.9, 22.7, 22.6, 21.0, 20.6, 19.7, 19.6, 13.0, 12.2, 11.8.

4.10. Compound 13

Compound **8** (10.5 mg, 7.5 μmol) was coevaporated with dry toluene (1 mL × 3). Sodium azide (5.0 mg, 75 μmol, 10 equiv) was added and the mixture was dissolved in dry *N,N*-dimethylformamide (2 mL). The suspending solution was heated to 80 °C, stirred for 19 h and then cooled to rt. The solution was concentrated, diluted with ethyl acetate (20 mL), and washed with water (20 mL × 3). The aqueous layer was back extracted with toluene (20 mL) and the combined organic layer was dried over $MgSO_4$, filtered, and concentrated. To the crude product including **12**, **11** (14.2 mg, 30 μmol, 4 equiv) and copper powder (9.1 mg) were added. The mixed solvent (*t*-butanol–water (2:1, v/v, 3.0 mL)) was added to the mixture and the solution was stirred and heated to 65 °C. After 14 h, the solution was cooled to rt, filtered and purified by silica gel column chromatography (dichloromethane (3% to 4% methanol)) to afford the pure **13** as a colorless oil (9.0 mg, 4.9 μmol, 66%).

^{1}H NMR ($CDCl_3$) δ 8.02–7.60 (24H, N*Phth*), 7.49 (s, 1H, triazole-H), 5.69 (d, J = 8.7, 1H, H-1), 5.43 (d, J = 7.8, 1H, H-1), 4.83 (d, J = 7.8, 1H, H-1), 4.72 (s, 2H), 4.60 (m, 1H), 4.35–3.40 (m, 21H), 3.14–3.10 (m, 3H), 2.95 (d, J = 11.1, 1H), 2.58 (t, J = 6.6, 2H), 2.18–2.09 (s × 3, 9H), 1.88–0.80 (m, 40H).

^{13}C NMR (75.5 MHz, $CDCl_3$) δ 168.5, 168.2, 168.0, 148.0, 147.9, 144.4, 134.4, 133.9, 133.8, 132.1, 131.9, 131.7, 131.6, 131.5, 127.9, 126.0, 123.8, 123.5, 123.1, 122.9, 117.6, 99.5, 99.2, 98.5, 75.6, 74.8, 72.6, 72.2, 70.8, 69.6, 69.0, 68.5, 66.3, 65.6, 54.5, 54.1, 53.5, 47.0, 40.1, 39.8, 39.3, 37.5, 37.4, 37.3, 32.8, 32.7, 31.2, 30.2, 29.7, 28.0, 24.8, 24.4, 23.8, 22.7, 22.6, 21.0, 20.6, 19.7, 19.6, 12.9, 12.0, 11.8.

MALDI-TOF MS: *m/z* calcd for $C_{101}H_{107}N_9NaO_{24}$ $[M+Na]^+$: 1853.74 Found: 1852.79.

4.11. Compound 14

Compound **13** (3.9 mg, 2.1 μmol) was dissolved in ethanol (2.0 mL) and hydrazine monohydrate (60 μL) were added and the mixture was stirred and heated to 80 °C. After 4.5 h, the mixture was cooled to rt and concentrated. Eighth part of the entire crude product was purified by C4 reversed-phase HPLC (0.05% TFA, water-acetonitrile) and lyophilized from water to give **14** as a colorless solid (78.5 nmol, 29%).

MALDI-TOF MS: *m/z* calcd for $C_{53}H_{95}N_9NaO_{12}$ $[M+Na]^+$: 1072.70 Found: 1072.52.

4.12. Compound 16

Compound **15** (38.5 mg, 83 μmol) was coevaporated with dry toluene (10 mL × 4) and dissolved in dry tetrahydrofurane (1.5 mL). To the solution, sodium hydride (60% purity, 15.1 mg, 377 μmol, 4.5 equiv) and propargyl bromide (15 μL, 188 μmol, 2.3 equiv) were added. The mixture was heated to 60 °C and stirred for 16 h. After the solution was cooled to rt, methanol (1 mL) was added and concentrated. The crude product was dissolved in dichloromethane (30 mL) and washed with saturated brine (10 mL × 3) and the organic layer was dried over Na_2SO_4, filtered and concentrated. The crude product was dissolved in dry tetrahydrofurane (1.5 mL) and tetrabutylammonium fluoride (37.2 mg, 150 μmol) was added. After the solution was stirred for 20 min, the reaction was quenched by addition of saturated aqueous solution of $NaHCO_3$ and the solution was concentrated. The crude product was purified by silica gel column chromatography (dichloromethane-hexane (6:4, v/v)) to afford the pure **16** as a pale yellow oil (26.2 mg, 62 μmol, 75%).

^{1}H NMR ($CDCl_3$) δ 4.25 (s, 1H, Ar*OH*), 4.13 (d, J = 2.7, 2H, HC≡C*CH*$_2$O), 3.50 (t, J = 6.6, 2H, O*CH*$_2$CH$_2$), 2.59 (t, J = 6.9, Ar*CH*$_2$), 2.41 (t, J = 2.4, *HC*≡C), 2.15–2.10 (s × 2, 9H, Ar*CH3*), 1.81–1.22 (m, 21H).

^{13}C NMR (75.5 MHz, $CDCl_3$) δ 145.5, 144.5, 122.5, 121.0, 118.5, 117.3, 80.0, 74.4, 74.0, 70.3, 58.0, 39.4, 31.5, 30.1, 29.5, 29.5, 29.4, 26.0, 23.8, 23.6, 20.7, 12.2, 11.7, 11.3.

MALDI-TOF MS: *m/z* calcd for $C_{25}H_{39}O_3$ $[M+H]^+$: 387.3 Found: 386.8.

4.13. Compound 17

Compound **8** (4.5 mg, 3.2 μmol) was coevaporated with dry toluene (1 mL × 4), sodium azide (8.6 mg, 132 μmol, 41 equiv) was added and the mixture was dissolved in dry *N,N*-dimethylformamide (2.0 mL). The suspending solution was heated to 80 °C, stirred for 15 h and then cooled to rt. The solution was concentrated, dissolved in ethyl acetate (20 mL), and washed with water (20 mL × 3). The aqueous layer was back extracted with toluene (10 mL) and the combined organic layer was dried over $MgSO_4$, filtered, and concentrated. To the crude product including **12**, **16** (2.7 mg, 7.0 μmol, 2.2 equiv) and copper powder were added. Mixed solvent (*t*-butanol–water (2:1, v/v, 1.5 mL)) was added to the mixture and the solution was stirred and heated to 80 °C. After 3.5 h, the solution was cooled to rt, filtered and purified by silica gel column chromatography (dichloromethane (2.5–3.5% methanol)) to afford the pure **13** as a colorless oil (5.1 mg, 2.9 μmol, 91%).

^{1}H NMR ($CDCl_3$) δ 8.01–7.61 (24H, N*Phth*), 7.31 (s, 1H, triazole-H), 5.69 (d, J = 8.7, 1H, H-1), 5.44 (d, J = 8.4, 1H, H-1), 4.82 (d, J = 7.8, 1H, H-1), 4.63–4.56 (m, 1H), 4.50 (s, 2H), 4.40–3.37 (m, 26H), 3.13–3.07 (m, 3H), 2.91 (d, J = 11.1, 1H), 2.58 (t, J = 6.6, 2H), 2.14–2.10 (s × 3, 9H), 1.83–1.22 (m, 21H).

^{13}C NMR (75.5 MHz, $CDCl_3$) δ 168.6, 168.2, 168.0, 145.4, 144.8, 144.5, 134.5, 133.8, 132.1, 131.9, 131.5, 123.8, 123.5, 123.2, 122.5, 121.1, 118.6, 117.3, 99.4, 99.2, 98.4, 75.6, 74.5 72.6, 72.2, 70.7, 69.6, 69.0, 68.4, 65.4, 64.0, 54.5, 54.1, 53.5, 46.9, 39.9, 39.2, 37.5, 31.5, 30.1, 29.6, 29.5, 29.4, 26.1, 23.9, 23.5, 20.7, 12.3, 11.8, 11.3.

MALDI-TOF MS: *m/z* calcd for $C_{94}H_{93}N_9NaO_{25}$ $[M+Na]^+$: 1771.62 Found: 1770.43.

4.14. Compound 18

Compound **17** (5.1 mg, 2.9 μmol) was dissolved in ethanol (2.0 mL) and hydrazine monohydrate (60 μL) were added and the mixture was stirred and heated to 90 °C. After 4 h, the mixture was cooled to rt and concentrated. Four-twenty ninth of the entire crude product was purified by C18 reversed-phase HPLC (0.05% TFA, water–acetonitrile) and lyophilized from water to give **18** as colorless solid (235 nmol, 59%).

MALDI-TOF MS: *m/z* calcd for $C_{46}H_{81}N_9NaO_{13}$ $[M+Na]^+$: 990.59 Found: 990.49.

4.15. Compound 19

4-Monomethoxytrityl chloride (0.6416 g, 2.0 mmol) was dissolved in dry pyridine (20 mL) and stirred. To the solution, propargyl alcohol (150 μL, 2.54 mmol, 1.27 equiv) was added and stirred for 3 d. The solvent was evaporated. And the mixture was dissolved in dichloromethane (30 mL) and washed with saturated aqueous solution of $NaHCO_3$ (20 mL × 2). The aqueous layer was back extracted with dichloromethane (10 mL × 4). The combined organic layer was dried over Na_2SO_4, filtered and concentrated. The crude product was purified by silica gel column chromatography

(dichloromethane–hexane (3:1, v/v)) to afford the pure **19** as a colorless solid (0.5989 g, 1.82 mmol, 91%).

^{1}H NMR ($CDCl_3$) δ 7.49–7.45 (m, 4H, Ar), 7.37–7.20 (m, 8H, Ar), 6.87–6.82 (m, 2H, Ar), 3.80 (s, 3H, CH_3OAr), 3.75 (d, J = 2.4, HC≡CH_2), 2.39 (d, J = 2.4, HC≡CH_2).

^{13}C NMR ($CDCl_3$) δ 158.7, 143.8, 135.0, 130.2, 128.2, 127.9, 127.0, 113.2, 87.2, 80.5, 55.2, 52.7.

4.16. Compound 20

Compound **8** (4.2 mg, 3.0 μmol) was coevaporated with dry toluene (1 mL × 3), sodium azide (6.4 mg, 100 μmol, 33 equiv) was added and the mixture was dissolved in dry *N,N*-dimethylformamide (1.0 mL). The suspending solution was heated to 80 °C, stirred for 18 h and then cooled to rt. The solution was concentrated, dissolved in ethyl acetate (20 mL), and washed with water (20 mL × 3). The aqueous layer was back extracted with toluene (10 mL) and the combined organic layer was dried over $MgSO_4$, filtered, and concentrated. To the crude product including **12**, **19** (6.4 mg, 20 μmol, 6.7 equiv) and copper powder (3.8 mg) were added. Mixed solvent (*t*-butanol–water (2:1, v/v, 1.0 mL)) was added to the mixture and the solution was stirred and heated to 65 °C. After 12 h, the solution was cooled to rt, filtered and purified by silica gel column chromatography (dichloromethane (3% methanol)) to afford the pure **20** as a colorless oil (5.1 mg, 3.0 μmol, quant).

^{1}H NMR ($CDCl_3$) δ 8.04–7.23 (m, 37H, Ar), 6.84 (d, J = 9.0, 2H, Ar), 5.72 (d, J = 8.1, 1H, H-1), 5.49 (d, J = 8.1, 1H, H-1), 4.86 (d, J = 8.1, 1H, H-1), 4.62–4.55 (m, 1H), 4.35–3.42 (m, 26H), 3.21–3.03 (m, 3H), 2.80 (d, J = 11.7, 1H), 1.83–1.78 (m, 2H).

^{13}C NMR (75.5 MHz, $CDCl_3$) δ 168.6, 168.2, 167.9, 158.6, 145.5, 144.2, 135.4, 134.5, 134.0, 133.8, 132.1, 131.9, 131.7, 131.5, 130.3, 128.4, 127.9, 126.9, 124.1, 123.8, 123.6, 123.2, 122.3, 113.2, 99.3, 99.1, 98.5, 86.9, 78.5, 75.3, 72.7, 72.6, 72.3, 71.1, 69.7, 69.2, 68.3, 65.7, 58.6, 55.2, 54.5, 54.3, 53.6, 46.9, 39.8, 37.3, 30.1.

MALDI-TOF MS: m/z calcd for $C_{92}H_{75}N_9NaO_{24}$ $[M+Na]^+$: 1712.48 Found: 1712.16.

4.17. Compound 21

Compound **20** (5.1 mg, 3.0 μmol) was dissolved in dry ethanol (3.0 mL) and hydrazine monohydrate (90 μL) were added and the mixture was stirred and heated to 80 °C. After 4 h, the mixture was cooled to rt and concentrated. Eighth part of the entire crude product was purified by C18 reversed-phase HPLC (0.05% TFA, water–acetonitrile). A half of the purified product was dissolved in 80% aqueous solution of acetic acid (5 mL) and then the solvent was evaporated after 1.5 h. The product was dissolved to water (30 mL) and washed with dichloromethane (10 mL × 3). Water was evaporated and 1% aqueous solution of trifluoroacetic acid to the product. After coevaporation with water (2 mL × 3), the product was lyophilized from water to give **21** as a colorless solid (27 nmol, 14%).

MALDI-TOF MS: calcd for $C_{24}H_{47}N_9NaO_{11}$ m/z $[M+Na]^+$: 660.33 Found: 660.05.

4.18. Biological experiments

4.18.1. Cell culture

Rat hepatocellular carcinoma (McA-RH7777) cells were maintained in Dulbecco's modified Eagle's medium (Sigma–Aldrich, St Louis, MO) only or supplemented with 10% fetal bovine serum (Invitrogen, Carlsbad, CA), 100 units/ml penicillin, and 100 μg of streptomycin at 37 °C in 5% CO_2.

4.18.2. In vitro siRNA activity assay

To determine in vitro activity of siRNAs, McA-RH7777 cells (kindly gifted from Hiroyuki Arai, PhD) were transfected with 10 nM siRNAs in absence and presence of equally amount of compound **18** respectively using Lipofectamine™ 2000 (Invitrogen). The cells were harvested 24 h after transfection. Total RNA was extracted and the amount of endogenous *apoB* mRNA was measured by quantitative real-time polymerase chain reaction (qRT-PCR).

4.18.3. Quantitative RT-PCR assay

DNase-treated 2 μg of RNAs were reverse transcribed with Super Script III and Random Hexamers (Life Technologies, Carlsbad, CA). The cDNAs were amplified by the quantitative TaqMan system using the Light Cycler 480 Real-Time PCR Instrument (Roche Diagnostics, Mannheim, Germany). The primers and probes for rat *apoB* (NM_019287) and rat *glyceraldehyde-3-phosphate dehydrogenase* (*gapdh*; NM_017008) were designed by Applied Biosystems (Foster City, CA).

4.18.4. Statistical analysis

Student's two-tailed *t*-test was used to determine the significance of differences between control and transfected groups in quantitative RT-PCR assay. Data are presented as means ± standard error of the means (SEMs); P <0.05 was considered significant.

Acknowledgements

We thank the Japan Student Services Organization for the scholarship. And this work was supported by National Institute of Biomedical Innovation (NIBIO), KAKENHI (22·5612) and Japan Society for the Promotion of Science (JSPS).

Supplementary data

Supplementary data associated with this article can be found, in the online version, at http://dx.doi.org/10.1016/j.bmc.2013.12.060.

References and notes

1. Fire, A.; SiQun, X.; Mary, K. M.; Steven, A. K.; Samuel, E. D.; Craig, C. M. *Nature* **1998**, *391*, 806.
2. Davidson, B. L.; McCray, P. B. *Nat. Rev. Genet.* **2011**, *12*, 329.
3. Pecot, C. V.; Calin, G. A.; Coleman, R. L.; Lopez-Berestein, G.; Sood, A. K. *Nat. Rev. Cancer* **2011**, *11*, 59.
4. Kim, S.-S.; Garg, H.; Joshi, A.; Manjunath, N. *Trends Mol. Med.* **2009**, *15*, 491.
5. Castanotto, D.; Rossi, J. J. *Nature* **2009**, *457*, 426.
6. Rao, N. M. *Chem. Phys. Lipids* **2010**, *163*, 245.
7. Fröhlich, T.; Wagner, E. *Soft Matter* **2010**, *6*, 226.
8. Patil, M. L.; Zhang, M.; Betigeri, S.; Taratula, O.; He, H.; Minko, T. *Bioconjugate Chem.* **2008**, *19*, 1396.
9. Zhang, S.; Zhao, B.; Jiang, H.; Wang, B.; Ma, B. *J. Controlled Release* **2007**, *123*, 1.
10. Romøren, K.; Thu, B. J.; Bols, N. C.; Evensen, Ø. *Biochim. Biophys. Acta* **2004**, *1663*, 127.
11. Wightman, L.; Kircheis, R.; Rössler, V.; Carotta, S.; Ruzicka, R.; Kursa, M.; Wagner, E. *J. Gene Med.* **2001**, *3*, 362.
12. Iwata, R.; Sudo, M.; Nagafuji, K.; Wada, T. *J. Org. Chem.* **2011**, *76*, 5895.
13. Rigotti, A. *Mol. Aspects Med.* **2007**, *28*, 423.
14. Kappus, H.; Diplock, A. T. *Free Radical Biol. Med.* **1992**, *13*, 55.
15. Nishina, K.; Unno, T.; Uno, Y.; Kubodera, T.; Kanouchi, T.; Mizusawa, H.; Yokota, T. *Mol. Ther.* **2008**, *16*, 734.
16. Hosomi, A.; Arita, M.; Sato, Y.; Kiyose, C.; Ueda, T.; Igarashi, O.; Arai, H.; Inoue, K. *FEBS Lett.* **1997**, *409*, 105.
17. Nava, P.; Cecchini, M.; Chirico, S.; Gordon, H.; Morley, S.; Manor, D.; Atkinson, J. *Bioorg. Med. Chem.* **2006**, *14*, 3721.
18. Ito, H.; Ishida, H.; Kiso, M. *J. Carbohydr. Chem.* **2001**, *20*, 207.
19. Subramaniam, V.; Gurcha, S. S.; Besra, G. S.; Lowary, T. L. *Tetrahedron: Asymmetry* **2005**, *16*, 553.
20. Chang, R.; Moquist, P.; Finney, N. S. *Carbohydr. Res.* **2004**, *339*, 1531.
21. Brik, A.; Muldoon, J.; Lin, Y.-C.; Elder, J. H.; Goodsell, D. S.; Olson, A. J.; Fokin, V. V.; Sharpless, K. B.; Wong, C.-H. *ChemBioChem* **2003**, *4*, 1246.
22. Soutschek, J.; Akinc, A.; Bramlage, B.; Charisse, K.; Constien, R.; Donoghue, M., et al *Nature* **2004**, *432*, 173.

Journal of Controlled Release 178 (2014) 18–24

Contents lists available at ScienceDirect

Journal of Controlled Release

journal homepage: www.elsevier.com/locate/jconrel

Systemic siRNA delivery to a spontaneous pancreatic tumor model in transgenic mice by PEGylated calcium phosphate hybrid micelles

Frederico Pittella [a,b], Horacio Cabral [b], Yoshinori Maeda [b], Peng Mi [c], Sumiyo Watanabe [a], Hiroyasu Takemoto [c], Hyun Jin Kim [d], Nobuhiro Nishiyama [c], Kanjiro Miyata [a,*], Kazunori Kataoka [a,b,d,e,**]

[a] Center for Disease Biology and Integrative Medicine, Graduate School of Medicine, The University of Tokyo, 7-3-1 Hongo, Bunkyo-ku, Tokyo 113-0033, Japan
[b] Department of Bioengineering, Graduate School of Engineering, The University of Tokyo, 7-3-1 Hongo, Bunkyo-ku, Tokyo 113-8656, Japan
[c] Polymer Chemistry Division, Chemical Resources Laboratory, Tokyo Institute of Technology, R1-11, 4259 Nagatsuta, Midori-ku, Yokohama 226-8503, Japan
[d] Department of Materials Engineering, Graduate School of Engineering, The University of Tokyo, 7-3-1 Hongo, Bunkyo-ku, Tokyo 113-8656, Japan
[e] Center for NanoBio Integration, The University of Tokyo, 7-3-1 Hongo, Bunkyo-ku, Tokyo 113-8656, Japan

ARTICLE INFO

Article history:
Received 3 August 2013
Accepted 7 January 2014
Available online 15 January 2014

Keywords:
siRNA delivery
Calcium phosphate
PEG
Charge-conversional polymer
Transgenic mice
Spontaneous pancreatic carcinoma

ABSTRACT

Efficient systems for delivery of small interfering RNA (siRNA) are required for clinical application of RNA interference (RNAi) in cancer therapy. Herein, we developed a safe and efficient nanocarrier comprising poly(ethylene glycol)-*block*-charge-conversional polymer (PEG-CCP)/calcium phosphate (CaP) hybrid micelles for systemic delivery of siRNA and studied their efficacy in spontaneous bioluminescent pancreatic tumors from transgenic mice. PEG-CCP was engineered to provide the siRNA-loaded hybrid micelles with enhanced colloidal stability and biocompatibility due to the PEG capsule and with endosome-disrupting functionality due to the acidic pH-responsive CCP segment where the polyanionic structure could be converted to polycationic structure at acidic pH through *cis*-aconitic amide cleavage. The resulting hybrid micelles were confirmed to have a diameter of <50 nm, with a narrow size distribution. Intravenously injected hybrid micelles significantly reduced the luciferase-based luminescent signal from the spontaneous pancreatic tumors in an siRNA sequence-specific manner. The gene silencing activity of the hybrid micelles correlated with their preferential tumor accumulation, as indicated by fluorescence imaging and histological analysis. Moreover, there were no significant changes in hematological parameters in mice treated with the hybrid micelles. These results demonstrate the great potential of the hybrid micelles as siRNA carriers for RNAi-based cancer therapy.

1. Introduction

Small interfering ribonucleic acid (siRNA) provides new perspectives for the treatment of various diseases. It functions by obstructing a specific cellular process by reducing protein production in a sequence-specific manner, a phenomenon termed RNA interference (RNAi) [1–4]. In particular, the use of RNAi-based therapy is expected to have potential for treatment of cancer because cancerous cells overexpress several specific genes, including oncogenes [5,6]. In the development of an RNAi-based cancer therapy, systemic administration of siRNA is essential for its effective accumulation in the wide range of internal tumor tissues. However, intravenous injection of naked siRNA molecules results in their rapid enzymatic degradation and subsequent clearance through the kidneys [7,8]. Therefore, efficient carriers are required to ensure successful delivery of siRNA to the therapeutic site of action [3,6,9].

Calcium phosphate (CaP)-based nanocarriers, a promising delivery system, has been widely developed for delivering nucleic acids to mammalian cells [10–14]. These are readily prepared by mixing aqueous ionic solutions for efficient encapsulation of nucleic acids. In this regard, we have previously prepared poly(ethylene glycol) (PEG)-coated CaP hybrid micelles by utilizing PEG-polyanion block copolymers [12,15–20]. In these block copolymers, the polyanion segment acts as a binding moiety with CaP nanoparticles, whereas the PEG segment forms a nonionic and hydrophilic outer layer for enhanced colloidal stability and biocompatibility (Fig. 1A). Furthermore, our recent studies successfully demonstrated functionalization of the polyanion segment for efficient endosomal escape of the siRNA payload [19–21]. An acidic pH-responsive anionic moiety, *cis*-aconitic amide (Aco), was introduced into the cationic side chain of the endosome-disrupting polyaspartamide derivative, poly{*N*′-[*N*-(2-aminoethyl)-2-aminoethyl] aspartamide} (PAsp(DET)) (Fig. 1B). The obtained PAsp(DET-Aco) bearing a net negative charge was found to be inactive for membrane disruption at extracellular neutral pH. However, on reversion to the parent polycation PAsp(DET) by cleavage of the Aco moiety at endosomal acidic pH, membrane disruptivity was activated [thus, termed charge-conversional polymer (CCP)] (Fig. 1C) [22]. Ultimately, the systemic administration of PEG-CCP/CaP hybrid micelles carrying

* Corresponding author. Tel.: +81 3 5841 1701; fax: +81 3 5841 7139.
** Correspondence to: K. Kataoka, Center for Disease Biology and Integrative Medicine, Graduate School of Medicine, The University of Tokyo, 7-3-1 Hongo, Bunkyo-ku, Tokyo 113-0033, Japan. Tel.: +81 3 5841 7138; fax: +81 3 5841 7139.
E-mail addresses: miyata@bmw.t.u-tokyo.ac.jp (K. Miyata), kataoka@bmw.t.u-tokyo.ac.jp (K. Kataoka).

0168-3659/$ – see front matter © 2014 Elsevier B.V. All rights reserved.
http://dx.doi.org/10.1016/j.jconrel.2014.01.008

vascular endothelial growth factor (VEGF) siRNA achieved significant antitumor activity in a murine xenograft model of subcutaneous pancreatic tumors [20]. These results demonstrated the great potential of this system for use as a cancer therapy and motivated us to investigate this system further.

To confirm the translational capability of promising nanocarriers, relevant preclinical tumor models, which parallel the microenvironment characteristics of tumors in the clinic, should be considered. In animal tumor models prepared by implantation of exogenous cancer cells or tissues, the tumoral microenvironment presents substantial differences with that of tumors in patients, including stroma, vasculature, lymphatics, immune cells, and increased population of certain clonal fractions due to selective stresses during cell culture or tissue transplantation [23,24]. These features in transplanted models are expected to affect the nanocarrier-mediated delivery of siRNA as well as drugs, *e.g.*, efficiencies of penetration, accumulation, and gene silencing in tumor tissues. In this regard, in genetically engineered tumor models, the tumor development closely relates to the clinical setting of the disease, with immune responses, angiogenesis, and inflammation naturally interrelating with the tumor [23]. Therefore, by using such spontaneous tumor models, siRNA-loaded nanocarriers could be evaluated in tumors with more relevant microenvironment and cell populations.

In the present study, we applied siRNA-loaded hybrid micelles in a genetically engineered pancreatic tumor model, in which the tumor gradually arises *in situ* and is associated with normal immune, angiogenesis, and inflammatory processes. The EL1-Luc/TAg transgenic mice used in this study spontaneously develop bioluminescent pancreatic adenocarcinoma owing to the SV40 T and firefly luciferase transgene constructs, which are regulated by the rat EL1 promoter [25]. SV40 T alters molecular, physiological, and histological aspects comparable to the tumorigenesis of acinar cell carcinoma in humans. Moreover, EL1-Luc/TAg transgenic mice permit non-invasive tracing of tumors through bioluminescence imaging because the cancer cells exclusively express luciferase. Accordingly, *in vivo* RNAi activity of the hybrid micelles carrying luciferase siRNA (siLuc) was determined by quantifying the luminescent signal from the pancreatic tumors after intravenous injection. To verify the validity of the measured RNAi activity, the tumor accumulation profile of the hybrid micelles was further assessed. To the best of our knowledge, this is the first study to demonstrate the effective delivery of siRNA to a spontaneous tumor model in transgenic mice by systemic administration.

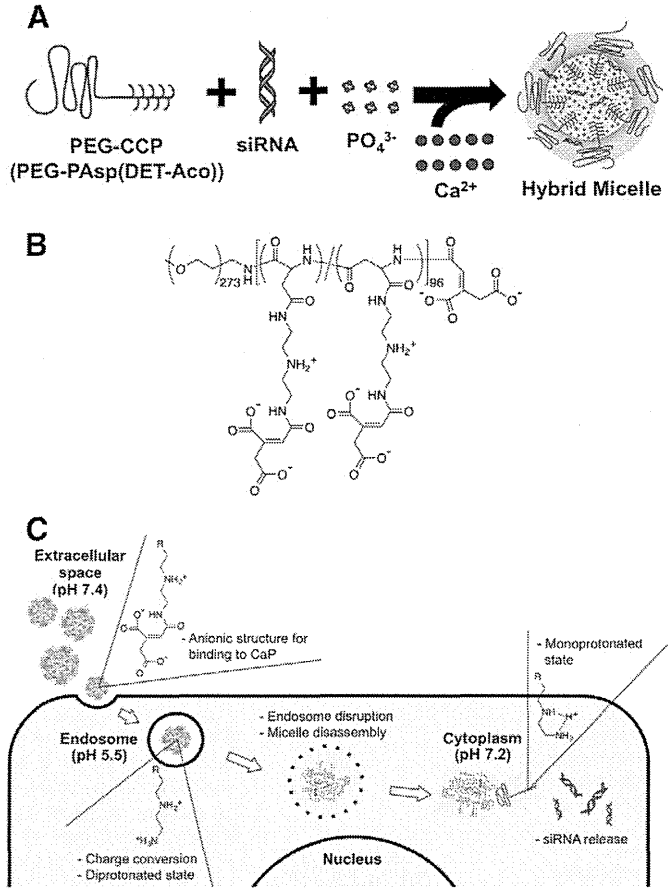

Fig. 1. (A) Schematic illustration of the preparation of hybrid micelles with PEG-CCP, siRNA, and CaP. (B) Chemical structure of PEG-PAsp(DET-Aco), termed PEG-CCP. (C) Schematic illustration of the cellular delivery of siRNA by PEG-CCP/CaP hybrid micelles. At extracellular neutral pH, PEG-CCP binds to the CaP nanoparticle, generating a PEG outer layer. Once endocytosed by the cell, the hybrid micelles undergo endosomal acidification. During acidification, PEG-CCP is converted to the parent PEG-PAsp(DET) through cleavage of the *cis*-aconitic amide bond, exposing the diprotonated side chain structure for endosomal membrane disruption. Finally, the siRNA payload is released into the cytoplasm, while the PAsp(DET) segment adopts the membrane-inactive monoprotonated side chain at cytoplasmic neutral pH.

2. Materials and methods

2.1. Materials, cell lines, and animals

$CaCl_2$ (anhydrous), Na_3PO_4, NaCl, HCl, ethanol, and phosphate buffered saline (PBS) were purchased from Wako Pure Chemical Industries Ltd. (Osaka, Japan). Dulbecco's modified Eagle's medium (DMEM) and penicillin/streptomycin stabilized solution were purchased from Sigma-Aldrich (St. Louis, MO). *In vivo* grade luciferin VivoGlo, cell culture lysis buffer, and the Luciferase Assay System were purchased from Promega Corporation (Madison, WI). Tissue-Tek OCT compound and fetal bovine serum (FBS) were acquired from Sakura Finetek USA, Inc. (Torrance, CA) and Dainippon Sumitomo Pharma Co., Ltd. (Osaka, Japan), respectively. Methoxy-poly(ethylene glycol)-*block*-poly(*N*″-{*N*′-[(*N*-*cis*-aconityl)-2-aminoethyl]-2-aminoethyl}aspartamide) (PEG-PAsp(DET-Aco) or PEG-CCP) was synthesized as previously described, and then characterized by ^{1}H NMR (PEG: 12 kDa; PAsp(DET-Aco): 34 kDa) [19,20]. Firefly luciferase siRNA (siLuc) and its control siRNA (siScr) were synthesized by Hokkaido System Science (Hokkaido, Japan). The sequences of the siLuc were: 5′-CUU ACG CUG AGU ACU UCG AdTdT-3′ (sense) and 5′-UCG AAG UAC UCA GCG UAA GdTdT-3′ (antisense); the sequences of the siScr were: 5′-UUC UCC GAA CGU GUC ACG UdTdT-3′ (sense) and 5′-ACG UGA CAC GUU CGG AGA AdTdT-3′ (antisense). Fluorescently labeled siLuc was obtained by introducing Alexa Fluor 647 to the 5′ end of sense strand from GeneDesign, Inc. (Osaka, Japan).

HeLa-Luc, a firefly luciferase-expressing human cervical cancer cell line, was purchased from Caliper Life Science (Hopkinton, MA). The cells were maintained in DMEM containing 10% FBS and 1% streptomycin/penicillin in a humidified atmosphere containing 5% CO_2 at 37 °C. FVB/NJc1 female mice (18–20 g, 6 weeks) were purchased from Clea Japan, Inc. (Tokyo, Japan). EL1-Luc/EL1-SV40 T-antigen transgenic mice (OncoMouse; male, 18–20 g, 6 weeks) were purchased from Caliper Life Sciences (Hopkinton, MA). Female FVB mice and male transgenic mice were allowed to breed, and the newborn mice were genotyped primarily by basal bioluminescence imaging at the age of 5 weeks. Male mice presenting basal luminescence in the pancreas were separated for use in the experiments. All animal experiments were performed in accordance with the Guidelines for the Care and Use of Laboratory Animals as stated by The University of Tokyo.

2.2. Preparation of hybrid micelles

Hybrid micelles were prepared as previously described [20]. In brief, a solution of 2.5 M $CaCl_2$ (1 μL) was diluted in 10 mM Tris buffer (pH 10) (11.5 μL). Another solution containing PEG-CCP (1.0 mg/mL) in 10 mM Tris/HCl buffer (pH 7.5) was mixed with a solution of 15 μM siRNA in 10 mM HEPES buffer (pH 7.2) and with 50 mM HEPES buffer containing 1.5

mM Na_3PO_4 and 140 mM NaCl (pH 7.5) (2.5 μL:5 μL:5 μL). The former solution was mixed with the latter solution by pipetting up and down for approximately 20 s (final siRNA concentration: 3 μM). The freshly prepared micelle solution containing 40 μg siRNA and 100 μg PEG-CCP (1 mL) was then purified and concentrated using a VivaSpin-06 device (molecular weight cut-off (MWCO): 10 kDa). The ultrafiltration was performed in a swing bucket rotor at 900 *g* and 4 °C for 20 min. To minimize non-specific binding of micelles to the membrane, the centrifuge filter devices were washed with de-ionized water before use. After centrifugation, the retained solution (100 μL) was added to 300 mM NaCl solution (100 μL) to adjust the final concentration to 150 mM NaCl. Through this procedure, the excess free calcium ions were removed from the micelle solution to the flow-through. The quantity of calcium removed was determined using a calcium sensitive dye, arsenazo III, by the SRL Laboratories (SRL Inc., Tokyo, Japan).

2.3. Transmission electron microscopic (TEM) imaging

Hybrid micelle solution (20 μL) was loaded on a 400-mesh copper grid and stained with 20 μL of uranyl acetate solution (2%, w/v) for 5 s. The copper grids with carbon-coated collodion film were glow-discharged for 10 s with an Eiko IB-3 ion coater (Eiko Engineering Co. Ltd., Japan) prior to use. The morphology of hybrid micelles was observed on a JEM-1400 (JEOL Ltd., Tokyo, Japan) with 100 kV acceleration voltage and 40 μA beam current, toward high resolution and high contrast with high performance imaging of specimens.

2.4. In vitro luciferase gene silencing

HeLa-Luc cells were seeded in a 96-well plate at a cell density of 2500 cells/well in 0.1 mL of DMEM containing 10% FBS and then pre-cultured for 24 h. Before transfection, the medium was refreshed. Hybrid micelles containing siRNA (siLuc or siScr), hybrid micelles without siRNA (mock), or naked siRNA (siLuc or siScr) were applied to each well to final siRNA concentrations of 100 and 200 nM (n = 6). After 48 h of incubation, the medium was removed and the cells were washed twice with 100 μL of PBS. The cells were then lysed with 50 μL of cell culture lysis buffer. The luciferase expression in the lysate was determined from photoluminescence intensity using the Luciferase Assay System and Mithras LB 940 (Berthold Technologies). The relative luciferase activity was calculated as a ratio to that in non-treated cells.

2.5. Biodistribution and tumor accumulation of hybrid micelles in transgenic mice

Mice were fed with alfalfa-free food *ad libitum*. A group of three male transgenic mice (15 weeks) were intravenously injected with Alexa Fluor 647-labeled siLuc (Alexa647-siLuc) contained in hybrid micelles (200 μL, 20 μg siRNA). As a control, the same amount of naked Alexa647-siLuc was also injected to another group of male transgenic mice. Intravenous injection was performed slowly (10 s per injection) to avoid adverse side effects. Mice were sacrificed 6 h after the injection, and then the main organs (heart, lungs, liver, spleen, kidneys, and pancreas, including tumors) were excised for fluorescent imaging using IVIS (Caliper Life Sciences, Hopkinton, MA). Organs were washed in PBS and kept on ice prior to analysis. Similarly, blood was collected from mice at 6 h after the injection, and then it was centrifuged at 2000 *g* for 10 min to obtain the plasma. The fluorescence intensity was determined using the Living Image software through the selection of an ROI around the whole organ/tumor and the plasma, and then it was converted to the % of dose/g of tissue (or plasma) based on a standard curve. To avoid incomplete separation of tumors from the pancreas, the combined weight of the organ and tumors was used for the subsequent statistical data analysis.

2.6. Tumor histology

After the biodistribution studies described in the preceding section were complete, a portion of the pancreas/tumor tissue from each mouse was rapidly frozen in Tissue-Tek OCT compound with liquid nitrogen in ethanol. The frozen pancreas/tumor tissues embedded in the block were then cut into 6-μm thick slices at −20 °C with a Tissue-Tek Cryo3 microtome/cryostat (Sakura Finetek USA, Inc., Torrance, CA). Each section of the pancreas/tumor tissue was fixed with formalin and stained with hematoxylin and eosin (HE) for histological identification of tumor cells and healthy pancreatic cells. In addition to HE staining, adjacent cryosections of the pancreas/tumor tissue were stained with Hoechst 33342 (Dojindo Lab., Kumamoto, Japan) for observation of cellular nuclei using a confocal laser scanning microscope (CLSM) (LSM 510, Carl Zeiss, Germany). The CLSM observation was performed at the excitation wavelengths of 633 nm (He–Ne laser) and 710 nm (MaiTai laser, two photon excitation) for Alexa647-siRNA and Hoechst 33342, respectively. The fluorescence intensities of the Alexa647-siRNA from the tumor region or the healthy pancreatic region in the obtained CLSM image were determined using the ImageJ software.

2.7. In vivo luminescence reduction in transgenic mice

Hybrid micelle solutions containing 20 μg of siLuc or siScr (200 μL) were slowly injected into the caudal vein of transgenic mice (13 weeks; n = 16). Bioluminescence intensity in the pancreatic tumors was determined before injection and 24 h after injection of the hybrid micelles using an IVIS instrument. Mice were anesthetized with isoflurane and luciferin was injected intraperitoneally at a dosage of 150 mg/kg (200 μL). Measurements were performed 10 min after luciferin injection for three different positions in each mouse (right flank, left flank, and ventral positions) to reduce variability in bioluminescence due to the tumor positions. Photons emitted from the pancreas region were quantified using the Living Image software and summed from the 3 positions. All images were set to the same conditions and color scale.

2.8. Hematological parameters and cytokine levels

Hybrid micelle solutions containing 20 μg of siScr (200 μL) were slowly injected in the caudal vein of female Balb/c mice (6 weeks). Blood was collected at several time points after the injection and centrifuged at 2000 *g* for 10 min to obtain the plasma. The levels of alkaline phosphatase (ALP), aspartate aminotransferase (AST), alanine aminotransferase (ALT), and creatinine (Cr) in the plasma were measured by the SRL Laboratories (SRL Inc., Tokyo, Japan) (n = 5). Also, the levels of tumor necrosis factor-α (TNF-α), interleukin-6 (IL-6), IL-1α, and IL-1β in plasma were determined by Quantikine® ELISA kits, according to the manufacturer's protocol (n = 4).

3. Results and discussion

3.1. Preparation of hybrid micelles

Preparation of CaP nanoparticles in an aqueous solution is known to result in the formation of insoluble large aggregates over time. Thus, PEG-CCP (Fig. 1B) was used to prepare CaP nanoparticles with enhanced colloidal stability through the steric repulsive effect of the PEG capsule. These nanoparticles also had endosome-disrupting functionality derived from the CCP segment. This segment was synthesized through the introduction of an Aco moiety into the side chain of PAsp(DET) through *cis*-aconitic amide bond formation. Successful preparation of PEG-CCP (or quantitative introduction of the Aco moiety) was confirmed using ^{1}H NMR spectroscopy (data not shown), as previously described [19]. The resulting PAsp(DET-Aco) segment was stable at neutral pH, whereas under acidic conditions, it underwent *cis*-aconitic amide cleavage to revert back to the parent PAsp(DET) (Fig. 1C) [22].

The generated PAsp(DET) enabled acidic pH-selective membrane disruption based on the distinctive change in the protonation state of the side chain unit, *i.e.*, the monoprotonated state at neutral pH and the diprotonated state at acidic pH, directed toward endosomal escape of the payload (Fig. 1C) [26,27].

The hybrid micelles were prepared by simple mixing of a solution containing PEG-CCP, siRNA, and phosphate ions, with a solution of calcium ions (Fig. 1A). The prepared micelles were then subjected to ultrafiltration (MWCO: 10 kDa) for the removal of excess free calcium ions as well as for concentration of the sample. The concentrated solution was diluted with the same volume of NaCl solution (300 mM) to generate the hybrid micelle solution at 150 mM NaCl. The obtained hybrid micelles were observed with a high performance TEM. Fig. 2A depicts spherical nanoparticles of approximately 30 nm in diameter with a clearly narrow size distribution, which was confirmed by the size distribution histogram obtained from analyses of the TEM images (mean diameter: 33.2 nm, n = 111) (Fig. 2B). The hybrid micelle solution was further characterized by dynamic light scattering (DLS) and electrophoretic light scattering. The size of hybrid micelles was 38 nm at the peak of the number-weighted histogram in DLS (Supporting Fig. S1), associated with a narrow size distribution (polydispersity index = 0.09). This size is consistent with that estimated from the TEM images. Further, the zeta-potential of hybrid micelles was almost neutral (−2.2 mV), consistent with the presence of nonionic PEG outer layer. In addition, the DLS analysis revealed that the cumulant size of the hybrid micelles was maintained over 7 days of storage at 4 °C (data not shown), demonstrating the potential for long-term storage in a refrigerator.

3.2. In vitro luciferase gene silencing

To confirm *in vitro* siRNA delivery efficacy, the hybrid micelles carrying siLuc were applied to a luciferase assay with cultured HeLa-Luc cells as a luciferase-expressing model cell line. After 48 h of incubation, siLuc delivered by the hybrid micelles significantly decreased the luciferase expression in a dose-dependent manner (Fig. 3); the hybrid micelles inhibited approximately 50% and 90% of luciferase expression at 100 nM and 200 nM siRNA, respectively. In sharp contrast, the hybrid micelles with a control sequence of siRNA (siScr) as well as the mock micelles without siRNA resulted in no reduction in luciferase expression, indicating sequence-specific, potent gene silencing ability of the hybrid micelles. In our previous studies, the hybrid micelles exhibited a significant gene silencing effect on endogenous VEGF in cultured pancreatic cancer cells (PanC-1 and BxPC3) [19,20], suggesting that their gene silencing ability is not limited to a specific target gene and cell line. The efficient gene silencing ability of the hybrid micelles was probably due to the stable encapsulation of siRNA in CaP nanoparticles in cell culture medium [20], followed by efficient cellular internalization and endosomal escape induced by the CCP segment [19]. With regard to the cellular internalization, our previous study revealed that hybrid micelles were efficiently uptaken by HeLa cells within 4 h, probably due to an energy-dependent endocytosis [16]. It should be noted that no significant cytotoxicity was observed for any of the samples at the tested concentrations, as determined in a cell viability assay using a water soluble tetrazolium salt (WST-8) (data not shown).

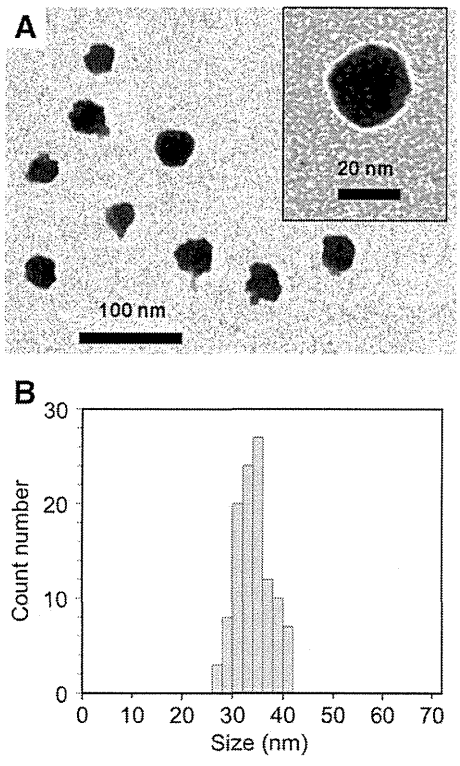

Fig. 2. (A) TEM image of the hybrid micelles. (B) Size distribution histogram of the hybrid micelles based on their TEM images.

3.3. Biodistribution and tumor accumulation of hybrid micelles in transgenic mice

Biodistribution of hybrid micelles after intravenous injection was evaluated in the transgenic mice presenting spontaneous pancreatic tumors using Alexa647-siRNA. At 6 h after injection, the transgenic mice were sacrificed, and the organs were excised for measuring fluorescence intensity, which was then converted to the % of dose/g of tissue based on a standard curve. As the border between a pancreatic tumor and healthy pancreas tissue is unclear, the fluorescence intensity of the whole pancreatic tissue was measured for tumor accumulation of Alexa647-siRNA. Note that the significant fluorescence was not detected from the collected blood samples, indicating that almost all the hybrid micelles (or Alexa647-siRNAs) were eliminated from the bloodstream within 6 h. Thus, the fluorescence intensity measured from each organ would not be affected by blood circulating micelles. As shown in Fig. 4, the amount of hybrid micelles was approximately 0.9% of dose/g of pancreas/tumor, which was 6-fold larger than that in naked siRNA. No significant difference between hybrid micelles and naked siRNA was observed for the accumulation in other organs; however, the kidneys displayed lower accumulation for Alexa647-siRNA delivered by the hybrid micelles compared to naked siRNA. These results suggest that the hybrid micelles could protect Alexa647-siRNA from rapid renal filtration, enabling it to circulate for longer in the blood, and therefore accumulate more in the pancreas/tumor.

The enhanced accumulation of hybrid micelles in the pancreas/tumor was further investigated by histological analysis. First, HE-stained sections were prepared to facilitate distinction of the tumor region (T) from healthy pancreatic tissue (H). As depicted in Fig. 5A, healthy pancreatic cells were organized into lobules toward formation of glandular acini. In contrast, tumor cells show a non-organized solid growth pattern [28,29]. Fig. 5A also shows the presence of connective tissue septa in between the T and H areas. CLSM was then performed to image the corresponding Hoechst 33342-stained sections. It is noteworthy that fluorescence signals from Alexa647-siRNA delivered by hybrid micelles were found mainly in the tumor region (Fig. 5B). Quantitative analysis using the ImageJ software indicated that the fluorescence signal of Alexa647-siRNA in the tumor region was 2.9-fold stronger than that in the healthy pancreas. By considering that the average weight of pancreas/tumor in the transgenic mice was 2.2-fold higher than that of pancreas in wild-type mice, the tumor accumulation of siRNA delivered by hybrid micelles can be roughly estimated to be ~1.3% of dose/g of tumor with the assumption that the tissue weights are similar between tumor and healthy pancreas in the transgenic mice. Thus, the

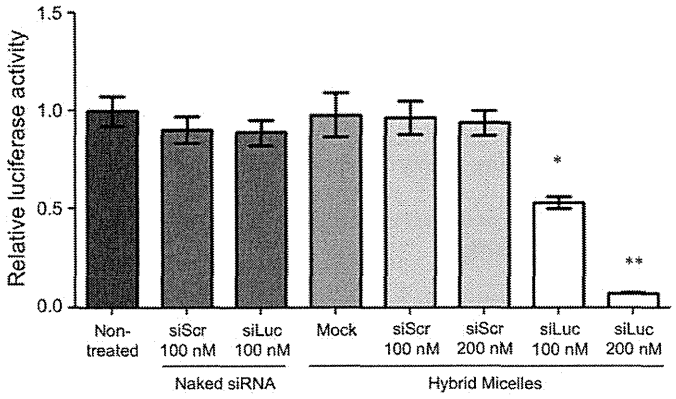

Fig. 3. *In vitro* luciferase gene silencing by hybrid micelles in cultured HeLa-Luc cells. Luciferase luminescence was quantified after 48 h of incubation of cells treated with samples. Results are expressed as mean and standard deviation (n = 6). *$P < 0.05$; **$P < 0.001$ (ANOVA followed by Newman–Keuls).

preferential tumor accumulation of siRNA-loaded hybrid micelles was demonstrated in the spontaneous pancreatic tumor model.

In a previous study, we reported that the tumor vasculature in the EL1-Luc/TAg transgenic mice was covered with pericytes [30], which can considerably limit the penetration of nanocarriers into the spontaneous tumor model in comparison to hypervascular and/or less stromal tumor models [31,32]. Nevertheless, the hybrid micelles apparently penetrated and distributed within the tumors (Fig. 5B). This behavior should be attributed to the relatively small size of the hybrid micelles (approximately 30–40 nm in diameter, Fig. 2 and Supporting Fig. S1), facilitating the passage of the nanocarriers through the tumor vasculature and stromal tissues. This was in agreement with our recent study where <50-nm polymeric micelles efficiently penetrated into the tissue, even in hypopermeable tumor models, which was in contrast to the control micelles that were >50 nm in size [33]. It should be further noted that the enhanced tumor accumulation behavior of hybrid micelles, compared to naked siRNA, in the present spontaneous pancreatic tumors was comparable to our previous observation in a subcutaneous BxPC3 tumor model [20]. This can also be explained by the small size of hybrid micelles, as the small-sized nanocarriers may be less affected by the tumor microenvironments restricting extravasation and penetration of nanocarriers, such as pericyte coverage of the vasculature [33]. Altogether, the hybrid micelles are a promising strategy for the systemic delivery of siRNA to various and whole tumor tissues/cells.

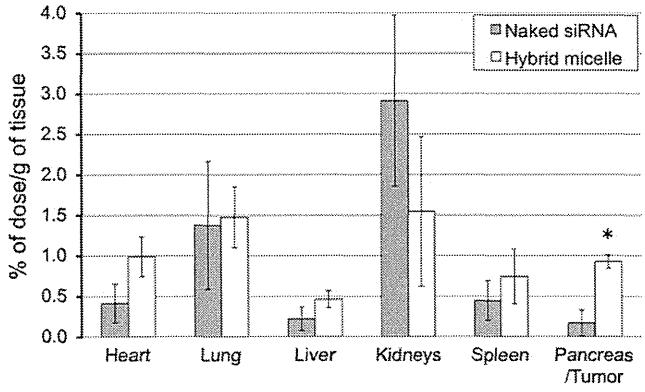

Fig. 4. Biodistribution of Alexa647-siRNA-loaded hybrid micelles and naked Alexa647-siRNA by fluorescence quantification at 6 h after intravenous injection (20 μg siRNA/injection) in 14-week-old transgenic mice. The obtained fluorescence intensities were converted to % of dose/g of tissue based on a standard curve. Results are expressed as mean and standard error of mean (n = 3). ANOVA followed by Newman–Keuls (*$P < 0.01$).

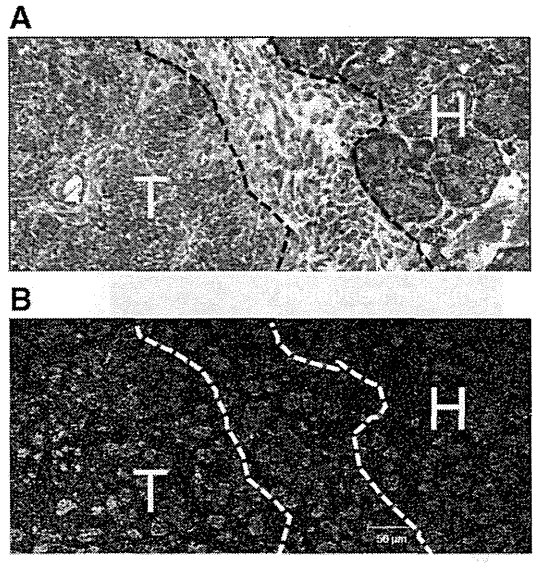

Fig. 5. Histological observation of pancreas/tumor in transgenic mice treated with hybrid micelles. Sections were prepared from the pancreas/tumor tissue excised at 6 h after intravenous injection of hybrid micelles carrying Alexa647-siRNA (20 μg siRNA/injection) to transgenic mice. (A) HE staining: non-organized tumor cells (T) and healthy pancreatic structure in lobes (H) are separated by the dotted line. (B) CLSM image of an adjacent section to that stained with HE. Nuclei (blue) were stained with Hoechst 33342, and Alexa647-siRNA is shown in green.

3.4. *In vivo* luciferase gene silencing in transgenic mice

Pancreatic cancer is considered to be one of the most fatal cancers [34]. Moreover, the all-stage 5-year survival has not improved greatly during the last 25 years [35]. These facts have motivated us to develop novel therapeutics to improve the prognosis of pancreatic cancer patients. An immunocompetent mouse presenting spontaneous pancreatic tumors is a useful model for establishment of such novel therapeutics, including anticancer drug-loaded micelles [30]. Herein, the *in vivo* gene silencing activity of hybrid micelles was evaluated with the spontaneous pancreatic tumor model developed in EL1-Luc/TAg transgenic mice, in which the expression of firefly luciferase is promoted specifically in the acinar cell carcinoma [25]. Accordingly, this model can be used for a gene silencing assay that employs the bioluminescence of the pancreatic tumors. It is worth noting that the following characteristics were confirmed for the spontaneous pancreatic cancer model in the previous study [30]; i) liver and intestine metastases are likely to occur in this model after the mice becoming 16 weeks old, ii) the pancreas/tumor in this model is enlarged and also the pancreatic cancer may grow over the normal position of pancreas, and iii) the bioluminescent signal from the pancreatic cancer is not always emitted from the same anatomic position. Considering these points, the bioluminescence measurements in this study were performed for 3 different positions, *i.e.*, left flank, frontal, and right flank of the 13-week-old mice without detectable tumor metastases.

Representative bioluminescence images of the left flank position of mice treated with or without siLuc-loaded hybrid micelles are shown in Fig. 6A, where the variable bioluminescence signals from the pancreatic tumor can be identified. At 24 h after systemic injection of the hybrid micelles, the bioluminescence intensity in the pancreatic tumors exhibited a significant reduction of 61% compared with the initial intensity before injection (Fig. 6B; $P < 0.01$), indicating that the hybrid micelles induced efficient luciferase gene silencing in the tumor tissue. There was no significant reduction in the bioluminescence signal after injection of siScr-loaded hybrid micelles, indicating that the reduction in the bioluminescence intensity was due to the sequence-specific

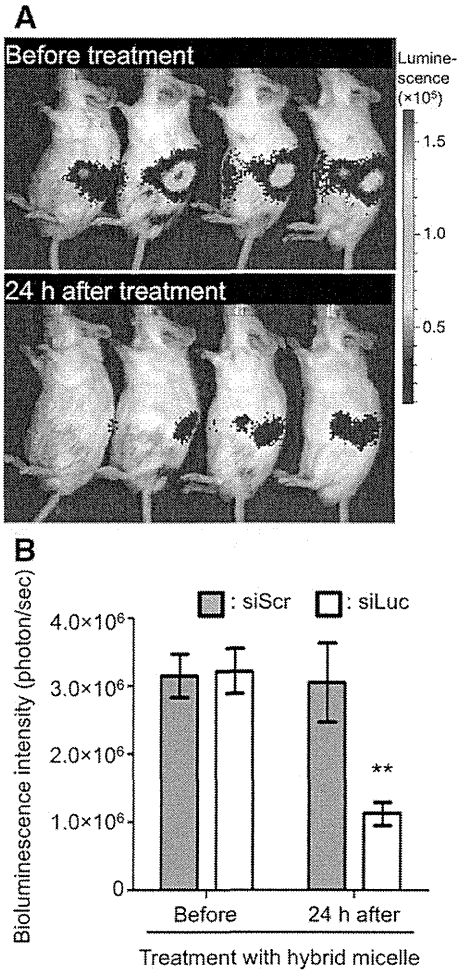

Fig. 6. *In vivo* gene silencing activity of systemically administered hybrid micelles in the spontaneous pancreatic tumors of transgenic mice. (A) Representative images of mice before and 24 h after injection of hybrid micelles containing siLuc (20 μg siRNA/mouse). (B) Bioluminescence intensity in the pancreatic tumors after intravenous injection of hybrid micelles containing siLuc or siScr (20 μg siRNA/mouse). Results are expressed as mean and standard deviation (n = 16). ANOVA followed by Newman–Keuls (**$P < 0.01$).

RNAi machinery. The similar gene silencing profile of hybrid micelles was further observed for the protein amount of luciferase in homogenized pancreas/tumor tissues (Supporting Fig. S2). This sequence-specific gene silencing activity of hybrid micelles is consistent with their significantly enhanced tumor accumulation of the siRNA payload (Figs. 4 and 5), which was roughly estimated to be ~1.3% of dose/g of tumor, corresponding to ~40 ng siRNA. Interestingly, the *in vivo* gene silencing efficacy of hybrid micelles in the spontaneous pancreatic cancer cells (60% with ~40 ng siRNA) was apparently higher than the *in vitro* efficacy in the cultured HeLa-Luc cells (50% with ~130 ng siRNA). These different efficacies might be due to varying cellular innate functions between the *in vivo* pancreatic cancer cells and the *in vitro* monolayer-cultured cervical cancer cells. The cellular innate functions, including the expression levels of luciferase and RNAi-related genes, are known to be substantially altered between live tissue and cell culture, especially monolayer culture, and also different types of cells [36–38]. Indeed, the luciferase expression in the present pancreatic cancer cells was lost in monolayer culture. This is the reason for the use of HeLa-Luc cells as a conventional cancer cell line for demonstrating the *in vitro* gene silencing activity of hybrid micelles.

3.5. Hematological parameters and cytokine levels after systemic administration of hybrid micelles

To verify the safety of the hybrid micelle formulation, hematological parameters and inflammatory cytokine levels were measured at several time points after systemic administration. As summarized in Table 1, the intravenous injection of hybrid micelles induced no remarkable changes in the levels of AST, ALT, and ALP as indicators of liver function and that of Cr as an indicator of kidney function over 48 h, suggesting negligible adverse side effects on the liver and the kidneys. Similarly, the levels of inflammatory cytokines, *i.e.*, TNF-α, IL-6, IL-1α, and IL-1β, were not affected by the injection of hybrid micelles (Supporting Fig. S3). Overall, it was demonstrated that the intravenous injection of hybrid micelles induced no severe acute toxicity under the tested conditions.

4. Conclusion

In the present study, hybrid micelles prepared with a smart block copolymer PEG-CCP were applied for systemic siRNA delivery to spontaneous pancreatic tumors in EL1-Luc/TAg transgenic mice. The obtained results confirmed the enhanced accumulation of siRNA-loaded hybrid micelles in the tumor tissue and their significant gene silencing activity. Notably, this was associated with negligible changes in hematological parameters. Altogether, the great potential of the hybrid micelles for RNAi-based cancer therapy was successfully demonstrated.

Acknowledgment

This research was funded by the Japan Society for the Promotion of Science (JSPS) through the "Funding Program for World-Leading Innovative R&D on Science and Technology (FIRST Program)," the Adaptable and Seamless Technology Transfer Program through Target-driven R&D (A-STEP), the National Institute of Biomedical Innovation (NIBIO), and Grants-in-Aid for Scientific Research from the Japanese Ministry of Health, Labour and Welfare. Part of this work was conducted in the Research Hub for Advanced Nano Characterization, The University of Tokyo, supported by the Ministry of Education, Culture, Sports, Science and Technology (MEXT), Japan. The authors are grateful to S. Ogura and K. Date for their assistance with animal care.

Appendix A. Supplementary data

Supplementary data to this article can be found online at http://dx.doi.org/10.1016/j.jconrel.2014.01.008.

References

[1] A. Fire, S. Xu, M.K. Montgomery, S.A. Kostas, S.E. Driver, C.C. Mello, Potent and specific genetic interference by double-stranded RNA in *Caenorhabditis elegans*, Nature 391 (1998) 806–811.

Table 1
Hematological parameters after intravenous injection of hybrid micelles (20 μg siRNA/mouse).

	Non-treated (0 min)	10 min	30 min	60 min	120 min	20 h	48 h
AST (U/L)	40 ± 5	38 ± 9	42 ± 4	40 ± 5	41 ± 5	36 ± 4	47 ± 7
ALT (U/L)	61 ± 18	62 ± 13	73 ± 5	67 ± 8	64 ± 12	86 ± 28	61 ± 23
ALP (U/L)	401 ± 25	401 ± 22	424 ± 10	378 ± 8	384 ± 23	377 ± 28	477 ± 37
Cr (mg/dL)	0.11 ± 0.01	0.11 ± 0.01	0.11 ± 0.01	0.10 ± 0.01	0.10 ± 0.01	0.10 ± 0.02	0.07 ± 0.01

Abbreviations: AST, aspartate aminotransferase; ALT, alanine aminotransferase; ALP, alkaline phosphatase; Cr, creatinine. Results are expressed as mean and standard deviation (n = 5).

[2] S.M. Elbashir, J. Harborth, W. Lendeckel, A. Yalcin, K. Weber, T. Tuschl, Duplexes of 21-nucleotide RNAs mediate RNA interference in cultured mammalian cells, Nature 411 (2001) 494–498.
[3] K. Whitehead, R. Langer, D. Anderson, Knocking down barriers: advances in siRNA delivery, Nat. Rev. Drug Discov. 8 (2009) 129–138.
[4] J.C. Burnett, J.J. Rossi, RNA-based therapeutics: current progress and future prospects, Chem. Biol. 19 (2012) 60–71.
[5] F. Takeshita, T. Ochiya, Therapeutic potential of RNA interference against cancer, Cancer Sci. 97 (2006) 689–696.
[6] Y.-K. Oh, T.G. Park, siRNA delivery systems for cancer treatment, Adv. Drug Deliv. Rev. 61 (2009) 850–862.
[7] F. van de Water, O. Boerman, A. Wouterse, J. Peters, F. Russel, R. Masereeuw, Intravenously administered short interfering RNA accumulates in the kidney and selectively suppresses gene function in renal proximal tubules, Drug Metab. Dispos. 34 (2006) 1393–1397.
[8] J. Turner, S. Jones, S. Moschos, M. Lindsay, M. Gait, MALDI-TOF mass spectral analysis of siRNA degradation in serum confirms an RNase A-like activity, Mol. Biosyst. 3 (2007) 43–50.
[9] R.J. Christie, N. Nishiyama, K. Kataoka, Delivering the code: polyplex carriers for deoxyribonucleic acid and ribonucleic acid interference therapies, Endocrinology 151 (2010) 466–473.
[10] C.A. Chen, H. Okayama, Calcium phosphate-mediated gene-transfer—a highly efficient transfection system for stably transforming cells with plasmid DNA, Biotechniques 6 (1988) 632.
[11] M. Jordan, A. Schallhorn, F.M. Wurm, Transfecting mammalian cells: optimization of critical parameters affecting calcium-phosphate precipitate formation, Nucleic Acids Res. 24 (1996) 596–601.
[12] Y. Kakizawa, K. Kataoka, Block copolymer self-assembly into monodispersive nanoparticles with hybrid core of antisense DNA and calcium phosphate, Langmuir 18 (2002) 4539–4543.
[13] M. Zhang, K. Kataoka, Nano-structured composites based on calcium phosphate for cellular delivery of therapeutic and diagnostic agents, Nano Today 4 (2009) 508–517.
[14] J. Li, Y.C. Chen, Y.C. Tseng, S. Mozumdar, L. Huang, Biodegradable calcium phosphate nanoparticle with lipid coating for systemic siRNA delivery, J. Control. Release 142 (2010) 416–421.
[15] Y. Kakizawa, K. Miyata, S. Furukawa, K. Kataoka, Size-controlled formation of a calcium phosphate-based organic–inorganic hybrid vector for gene delivery using poly(ethylene glycol)-block-poly(aspartic acid), Adv. Mater. 16 (2004) 699–702.
[16] Y. Kakizawa, S. Furukawa, K. Kataoka, Block copolymer-coated calcium phosphate nanoparticles sensing intracellular environment for oligodeoxynucleotide and siRNA delivery, J. Control. Release 97 (2004) 345–356.
[17] Y. Kakizawa, S. Furukawa, A. Ishii, K. Kataoka, Organic–inorganic hybrid-nanocarrier of siRNA constructing through the self-assembly of calcium phosphate and PEG-based block aniomer, J. Control. Release 111 (2006) 368–370.
[18] M. Zhang, A. Ishii, N. Nishiyama, S. Matsumoto, T. Ishii, Y. Yamasaki, K. Kataoka, PEGylated calcium phosphate nanocomposites as smart environment-sensitive carriers for siRNA delivery, Adv. Mater. 21 (2009) 3520–3525.
[19] F. Pittella, M. Zhang, Y. Lee, H.J. Kim, T. Tockary, K. Osada, T. Ishii, K. Miyata, N. Nishiyama, K. Kataoka, Enhanced endosomal escape of siRNA-incorporating hybrid nanoparticles from calcium phosphate and PEG-block charge-conversional polymer for efficient gene knockdown with negligible cytotoxicity, Biomaterials 32 (2011) 3106–3114.
[20] F. Pittella, K. Miyata, Y. Maeda, T. Suma, Q. Chen, R.J. Christie, K. Osada, N. Nishiyama, K. Kataoka, Pancreatic cancer therapy by systemic administration of VEGF siRNA contained in calcium phosphate/charge-conversional polymer hybrid nanoparticles, J. Control. Release 161 (2012) 868–874.
[21] H. Takemoto, K. Miyata, S. Hattori, T. Ishii, T. Suma, S. Uchida, N. Nishiyama, K. Kataoka, Acidic pH-responsive siRNA conjugate for reversible carrier stability and accelerated endosomal escape with reduced IFNα-associated immune response, Angew. Chem. Int. Ed. 52 (2013) 6218–6221.
[22] Y. Lee, K. Miyata, M. Oba, T. Ishii, S. Fukushima, M. Han, H. Koyama, N. Nishiyama, K. Kataoka, Charge conversion ternary polyplex with endosomes disruption moiety: a technique for efficient and safe gene delivery, Angew. Chem. Int. Ed. 120 (2008) 5241–5244.
[23] K.K. Frese, D.A. Tuveson, Maximizing mouse cancer models, Nat. Rev. Cancer 7 (2007) 654–658.
[24] G. Francia, W. Cruz-Munoz, S. Man, P. Xu, R.S. Kerbe, Mouse models of advanced spontaneous metastasis for experimental therapeutics, Nat. Rev. Cancer 11 (2011) 135–141.
[25] N. Zhang, S. Lyons, E. Lim, P. Lassota, A spontaneous acinar cell carcinoma model for monitoring progression of pancreatic lesions and response to treatment through noninvasive bioluminescence imaging, Clin. Cancer Res. 15 (2009) 4915–4924.
[26] K. Miyata, M. Oba, M. Nakanishi, S. Fukushima, Y. Yamasaki, H. Koyama, N. Nishiyama, K. Kataoka, Polyplexes from poly(aspartamide) bearing 1,2-diaminoethane side chains induce pH-selective, endosomal membrane destabilization with amplified transfection and negligible cytotoxicity, J. Am. Chem. Soc. 130 (2008) 16287–16294.
[27] K. Miyata, N. Nishiyama, K. Kataoka, Rational design of smart supramolecular assemblies for gene delivery: chemical challenges in the creation of artificial viruses, Chem. Soc. Rev. 41 (2012) 2562–2574.
[28] L.A. Aaltonen, S.R. Hamilton, World Health Organization; international agency for research on cancer, in: L.A. Aaltonen, S.R. Hamilton (Eds.), Pathology and Genetics of Tumours of the Digestive System, IARC Press: Oxford University Press, Lyon: Oxford, 2000, (314 pp.).
[29] R.A. Caruso, A. Inferrera, G. Tuccari, G. Barresi, Acinar cell carcinoma of the pancreas, a histologic, immunocytochemical and ultrastructural study, Histol. Histopathol. 9 (1994) 53–58.
[30] H. Cabral, M. Murakami, H. Hojo, Y. Terada, M.R. Kano, U.-I. Chung, N. Nishiyama, K. Kataoka, Targeted therapy of spontaneous murine pancreatic tumors by polymeric micelles prolongs survival and prevents peritoneal metastasis, Proc. Natl. Acad. Sci. U. S. A. 110 (2013) 11397–11402.
[31] M.R. Kano, Y. Bae, C. Iwata, Y. Morishita, M. Yashiro, M. Oka, T. Fujii, A. Komuro, K. Kiyono, M. Kaminishi, K. Hirakawa, Y. Ouchi, N. Nishiyama, K. Kataoka, K. Miyazono, Improvement of cancer-targeting therapy, using nanocarriers for intractable solid tumors by inhibition of TGF-β signaling, Proc. Natl. Acad. Sci. U. S. A. 104 (2007) 3460–3465.
[32] L. Zhang, H. Nishihara, M.R. Kano, Pericyte-coverage of human tumor vasculature and nanoparticle permeability, Biol. Pharm. Bull. 35 (2012) 761–766.
[33] H. Cabral, Y. Matsumoto, K. Mizuno, Q. Chen, M. Murakami, M. Kimura, Y. Terada, M.R. Kano, K. Miyazono, M. Uesaka, N. Nishiyama, K. Kataoka, Accumulation of sub-100 nm polymeric micelles in poorly permeable tumours depends on size, Nat. Nanotechnol. 6 (2011) 815–823.
[34] American Cancer Society, Cancer Facts & Figs. 2011, Epidemiologic Surveillance Report, American Cancer Society, Atlanta, 2011, (available at: <http://www.cancer.org/acs/groups/content/@epidemiologysurveilance/documents/document/acspc-029771.pdf>. Accessed April 2013).
[35] A. Jemal, R. Siegel, J. Xu, E. Ward, Cancer statistics, 2010, CA Cancer J. Clin. 260 (2010) 277–300.
[36] F. Pampaloni, E.G. Reynaud, E.H.K. Stelzer, The third dimension bridges the gap between cell culture and live tissue, Nat. Rev. Mol. Cell Biol. 8 (2007) 839–845.
[37] N.J. Yoo, S.Y. Hur, M.S. Kim, J.Y. Lee, S.H. Lee, Immunohistochemical analysis of RNA-induced silencing complex-related proteins AGO2 and TNRC6A in prostate and esophageal cancers, APMIS 118 (2010) 271–276.
[38] T. Endo, K. Itaka, M. Shioyama, S. Uchida, K. Kataoka, Gene transfection to spheroid culture system on micropatterned culture plate by polyplex nanomicelle: a novel platform of genetically-modified cell transplantation, Drug Deliv. Transl. Res. 2 (2012) 398–405.

siRNA Conjugates

DOI: 10.1002/anie.201300178

Acidic pH-Responsive siRNA Conjugate for Reversible Carrier Stability and Accelerated Endosomal Escape with Reduced IFNα-Associated Immune Response**

Hiroyasu Takemoto, Kanjiro Miyata, Shota Hattori, Takehiko Ishii, Tomoya Suma, Satoshi Uchida, Nobuhiro Nishiyama, and Kazunori Kataoka**

Small interfering RNA (siRNA) has garnered much interest as a potential drug because of its strong gene-silencing activity.[1] Toward the success in siRNA therapeutics, many strategies have been developed for efficient siRNA delivery into the cytosol of target cells.[2] Among them, siRNA conjugates have arisen as one of the promising strategies in siRNA delivery, as siRNA can be readily conjugated to a functional molecule to acquire the ability of "programmed transfer" to the target sites.[3] Indeed, several ligand molecules, such as lactose and RGD peptide, were conjugated with siRNA for site- (or cell)-specific delivery.[3] Furthermore, multimolecular siRNA conjugates enable stable polyion complex (PIC) formation because of the increased electrostatic interactions with polycations, leading to facilitated cellular uptake through charge neutralization of siRNA and also protection of siRNA from enzymatic degradations.[4] However, those siRNA conjugates potentially stimulate immune responses through the activation of toll-like receptor 3 and/or protein kinase R,[4,5] and thus they are desired to disintegrate into monomeric siRNAs (mono-siRNAs) in the cell for reduced immune responses.[4] Meanwhile, considering that macromolecular drugs, including siRNA and its conjugates, would be taken up by cells through endocytosis and then delivered to the late endosome toward lysosomal degradation, siRNA needs to escape from the endosome into the cytosol for efficient gene silencing.[6] Therefore, design of a smart siRNA conjugate for programmed endosomal escape and release of mono-siRNA is a great challenge for successful siRNA delivery.

Herein, we developed a smart siRNA conjugate to fulfill the multifunctionality desired for enhanced siRNA delivery with reduced immunogenicity; that is, reversible PIC stability, endosomal escapability, and mono-siRNA releasability, based on a single chemical process. It is known that maleic acid amide (MAA) is relatively stable at extracellular neutral pH, while rapidly hydrolyzed at endosomal acidic pH.[7] Thus, we utilized this MAA chemistry as an acid-labile anionic moiety for linking siRNA to an endosome-disrupting polycation and concurrently converting the cationic sites into a biologically inert anionic derivative.[8] In design, the MAA-based conjugate is expected to improve the PIC stability through increased electrostatic interaction, while degrading the MAA moieties in the endosome for triggering three actions: 1) complex destabilization through unbalanced charges within PICs; 2) endosome disruption with the regenerated parent polycation; and 3) mono-siRNA release by MAA cleavage (Figure 1a). Figure 1b shows the chemical structure of siRNA-releasable/endosome-disrupting conjugate (REC), in which several siRNA molecules are grafted into the endosome-disrupting polymer side chains by the MAA linkage. The parent polycation is a polyaspartamide derivative with two repeating units of aminoethylene in each side chain (termed PAsp(DET)), which destabilizes the endosomal membrane integrity with the cationic diprotonated side chains to accelerate endosomal escape of the payload.[9]

A precursor polyanion was synthesized from PAsp(DET) to have a dibenzyl cyclooctyne (DBCO) group by MAA linkage as a conjugation site for siRNA. Then, an azide-modified siRNA (azide-siRNA) was reacted with the DBCO group in the polyanion side chains. Notably, the size exclusion chromatography (Supporting Information, Figure S5) confirmed that more than 95% of azide-siRNAs were conjugated to the polymer backbone utilizing a freeze–thaw treatment for the generation of a highly concentrated reactant phase.[10] This successful conjugation at the quite high rate allows the use of the obtained conjugate without further purification. As a result, about 30% of DBCO groups in the polymer side chains reacted with azide-siRNA; that is, about 5 siRNAs contained in the conjugate (Figure 1b). To investigate the

[*] H. Takemoto, Dr. K. Kataoka
Department of Materials Engineering, The University of Tokyo
Hongo 7-3-1, Bunkyo-ku, Tokyo 113-8656 (Japan)
E-mail: kataoka@bmw.t.u-tokyo.ac.jp
Homepage: http://www.bmw.t.u-tokyo.ac.jp/
S. Hattori, Dr. T. Ishii, T. Suma
Department of Bioengineering, The University of Tokyo
Hongo 7-3-1, Bunkyo-ku, Tokyo 113-8656 (Japan)
Dr. K. Miyata, S. Uchida
Division of Clinical Biotechnology, Center for Disease Biology and Integrative Medicine, The University of Tokyo
Hongo 7-3-1, Bunkyo-ku, Tokyo 113-0033 (Japan)
E-mail: miyata@bmw.t.u-tokyo.ac.jp
Dr. N. Nishiyama
Polymer Chemistry Division, Chemical Resources Laboratory
Tokyo Institute of Technology, R1-11
4259 Nagatsuta, Midori-ku, Yokohama 226-8503 (Japan)

[**] This research is supported by the Japan Society for the Promotion of Science (JSPS) through the "Funding Program for World-Leading Innovative R&D on Science and Technology (FIRST Program)," and Health and Labour Sciences Research Grants Research on Medical Device Development, Ministry of Health, Labour and Welfare. H.T. thanks the Research Fellowships of the Japan Society for the Promotion of Science for Young Scientists (JSPS).

Supporting information for this article is available on the WWW under http://dx.doi.org/10.1002/anie.201300178.

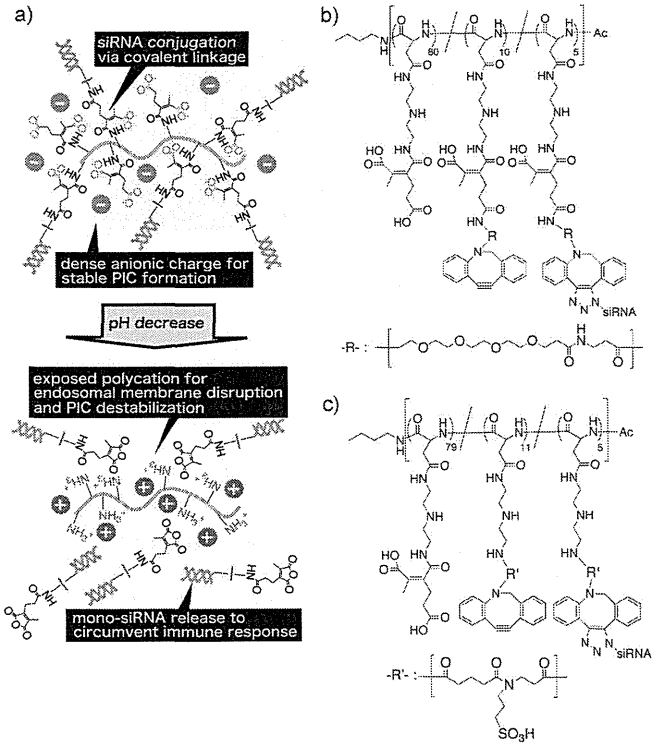

Figure 1. a) Illustration of releasable/enzyme-disrupting conjugate (REC) with the multifunctionality toward endosomal escape and release of mono-siRNA. b) Chemical structure of REC. c) Chemical structure of uREC. The PAsp derivative in this study has the mixed sequence of α and β isomers. Only α isomers are depicted in (b) and (c) for simplicity.

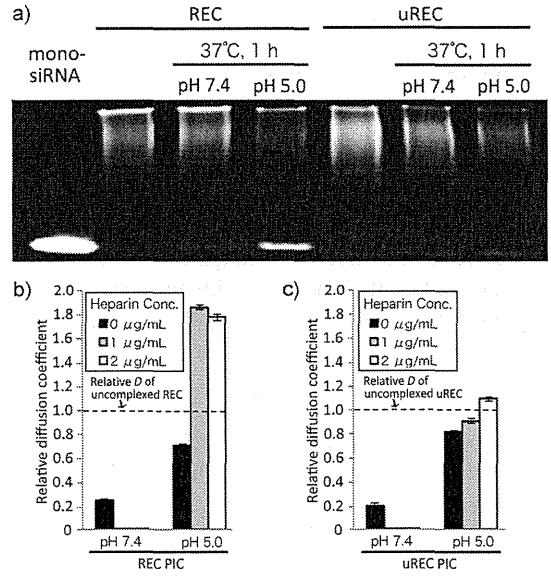

Figure 2. a) PAGE analysis of REC and uREC before and after 1 h incubation at 37 °C and at pH 7.4 or pH 5.0. b),c) Relative *D* values of siRNA conjugate PICs after a 30 min incubation at 37 °C with various heparin concentrations at pH 7.4 or pH 5.0. Relative *D* values are calculated by normalization of *D* to that of uncomplexed siRNA conjugates; REC PIC (b) and uREC PIC (c). Results were shown as mean and standard deviation obtained from 10 measurements.

effect of MAA linkage on the siRNA releasability, another siRNA conjugate, in which the DBCO group was directly conjugated to primary amines in PAsp(DET) without MAA linkage, was also synthesized as an siRNA-unreleasable but endosome-disrupting control (uREC; Figure 1c). The obtained siRNA conjugates were analyzed for their pH-sensitivity by polyacrylamide gel electrophoresis (PAGE) analysis (Figure 2a). The retarded bands in siRNA conjugates, compared to mono-siRNA, indicate that both siRNA conjugates had significantly higher molecular weight than mono-siRNA. A 1 h incubation of REC at pH 5.0 resulted in the band appearance at the same position as mono-siRNA, whereas such band was not observed at pH 7.4, indicating that mono-siRNA release was triggered selectively at the acidic pH. In contrast, the band corresponding to mono-siRNA was not observed for uREC after a 1 h incubation at both pHs of 5.0 and 7.4, indicating the essential role of MAA linkage for mono-siRNA release from REC.

Next, siRNA conjugates were mixed with a polycation PAsp(DET) to form PICs at N/P 10 (residual molar ratio of amines of PAsp(DET) to phosphates of siRNA) for their facilitated cellular uptake. PIC formation with siRNA conjugates as well as mono-siRNA was confirmed by fluorescence correlation spectroscopy (FCS) using Cy3-labeled siRNA (Cy3-siRNA) and its conjugates (Supporting Information, Table S2) as well as agarose gel electrophoresis (Supporting Information, Figure S6). The diffusion coefficients *D* in 10 mM HEPES buffer (pH 7.4) were determined to be 66.2 $\mu m^2 s^{-1}$ for mono-siRNA PIC and 2.9 $\mu m^2 s^{-1}$ for both siRNA conjugate PICs. These values were significantly smaller than those of the uncomplexed controls; that is, mono-siRNA (94.5 $\mu m^2 s^{-1}$) and siRNA conjugates (15.5 $\mu m^2 s^{-1}$ for REC and 18.8 $\mu m^2 s^{-1}$ for uREC). Considering that the *D* value of nanoparticles is inversely correlated with their size,[11] the smaller *D* values in the presence of polycation indicate successful PIC formation with the siRNA conjugates as well as mono-siRNA in the aqueous condition (siRNA concentration: 100 nM). The substantially smaller *D* values of the conjugate PICs, compared to the mono-siRNA PIC, indicate a larger association number of siRNA in the conjugate PICs, which is presumably due to increased anionic charges in the conjugate. Then, the acidic pH-sensitive PIC stability was further evaluated by FCS after a 30 min incubation of PICs at 37 °C in 10 mM HEPES (pH 7.4) and 10 mM MES (pH 5.0) containing heparin. Heparin is a major component of extracellular matrices on cellular surface and probably serves as a strong polyanionic counterpart to induce PIC dissociation.[12] The obtained *D* values of each sample were normalized to that of the corresponding uncomplexed siRNA control; that is, uncomplexed REC for REC PIC, uncomplexed uREC for uREC PIC, and uncomplexed mono-siRNA for mono-siRNA PIC (Figure 2b,c; Supporting Information, Figure S7, respectively). After incubation with heparin, a relative *D* of mono-siRNA PICs progressively increased with the increase in heparin concentration similarly at both pH values of 7.4 and 5.0, indicating that mono-siRNA PICs gradually dissociated with the increased counter polyanion, regardless of the environmental pH (Supporting Information, Figure S7). In contrast, relative *D* values of

REC and uREC PICs decreased after incubation with heparin at pH 7.4, suggesting that the conjugated siRNA is more stably encapsulated within PICs, compared to mono-siRNA, even after binding of heparin onto PIC surface. Notably, the incubation of REC and uREC PICs at pH 5.0 dramatically increased their relative *D* values, and furthermore, the increase in the relative *D* values was facilitated in the presence of heparin, indicating the acidic pH-responsive destabilization of the siRNA conjugate PICs (Figure 2b,c). Considering the fact that the MAA linkage contained in both siRNA conjugates can degrade at pH 5.0 to generate the polycations in PIC, the destabilization of siRNA conjugate PICs at pH 5.0 is presumably due to the electrostatic repulsion between the generated polycations and the originally incorporated polycations in PIC. Furthermore, the increased relative *D* values of REC PICs in the presence of heparin, beyond that of uncomplexed REC, strongly suggest the mono-siRNA release triggered by the cleavage of MAA linkage. These results demonstrate that the acidic pH-sensitivity of the MAA-based conjugates can be maintained even after PIC formation, and also they provide siRNA PICs with a reversible stability in response to the intracellular environment.

Delivery functionalities of REC PICs, namely cellular uptake efficiency and intracellular trafficking profile, were evaluated with cultured human ovarian cancer cells stably expressing luciferase (SKOV3-Luc). Cellular uptake of siRNA was estimated using Cy3-siRNA with a fluorescence microscopy (Supporting Information, Figure S8). REC and uREC PICs (N/P 10) allowed 30% increase in Cy3 fluorescence from cells compared to mono-siRNA PICs (N/P 10, $p < 0.005$), indicating that the conjugate formulation significantly enhanced the cellular uptake of siRNA is probably due to the higher stability, as suggested by the FCS result at pH 7.4 (Figure 2b,c; Supporting Information, Figure S7). Next, confocal laser scanning microscopic (CLSM) observation was performed to examine subcellular distribution of siRNA PICs (N/P 10), especially focusing on the colocalization of siRNA with the late endosome/lysosome as an indicator for endosomal entrapment (Figure 3a–c).[13] In the cells treated with mono-siRNA PICs, the colocalization (yellow) ratio of Cy3-siRNA (red) with a late endosome/lysosome marker LysoSensor Green (green) was increased up to 70% for the initial 12 h and then kept constant for subsequent 36 h (Figure 3d). In contrast, the cells treated with REC and uREC PICs showed that the colocalization ratio was progressively decreased over incubation period and reached about 30% after a 48 h incubation. The significantly lower colocalization ratios (or less endosomal entrapment) of REC/uREC PICs strongly suggest more efficient endosomal escape of siRNA compared to mono-siRNA PICs (Figure 3d). This enhanced endosomal escape with REC and uREC is consistent with the endosome-disrupting functionality of the backbone polymer, which should be converted into the parent polycation PAsp(DET) in the acidic late endosome/lysosome for the membrane disruption, as suggested by a membrane disruption assay at pH 7.4 and 5.0 (Supporting Information, Figure S9).[8,9]

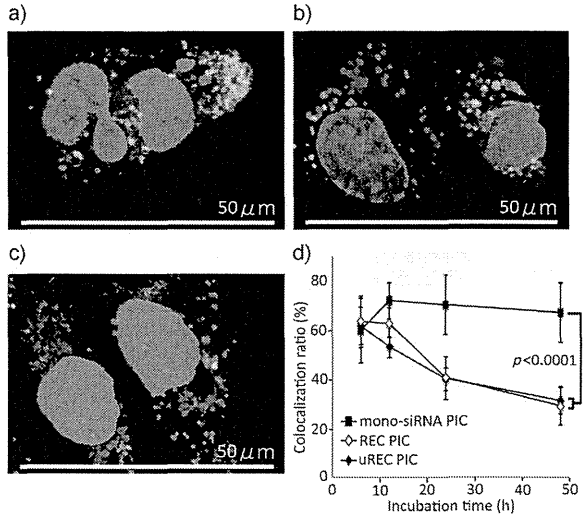

Figure 3. a–c) CLSM images 48 h after treatment of SKOV3-Luc cells with mono-siRNA PIC (a), REC PIC (b), and uREC PIC (c). Red Cy3-siRNA, green late endosome/lysosome (LysoSensor Green), blue nucleus (Hoechst 33342). A yellow pixel indicates colocalization between a red pixel and green pixel. d) Time-dependent change in the colocalization ratio between Cy3-siRNA and late endosome/lysosome. The colocalization ratio was shown as mean and standard deviation obtained from 10 cells. The *p* value was calculated according to Student's *t* test.

Next, the gene silencing ability of REC PICs was compared with mono-siRNA and uREC PICs by luciferase assay with cultured SKOV3-Luc cells (Figure 4a). Obviously, REC and uREC PICs achieved more efficient sequence-specific gene silencing in the cells than mono-siRNA PICs, which is presumably due to the enhanced endosomal escape of siRNA conjugate PICs (Figure 3) as well as facilitated cellular uptake of siRNA (Supporting Information, Figure S8). Interestingly, REC PICs induced significantly stronger gene silencing than uREC PICs ($p < 0.005$), demonstrating the positive effect of siRNA releasability by the MAA linkage on the siRNA delivery functionality. Mono-siRNA

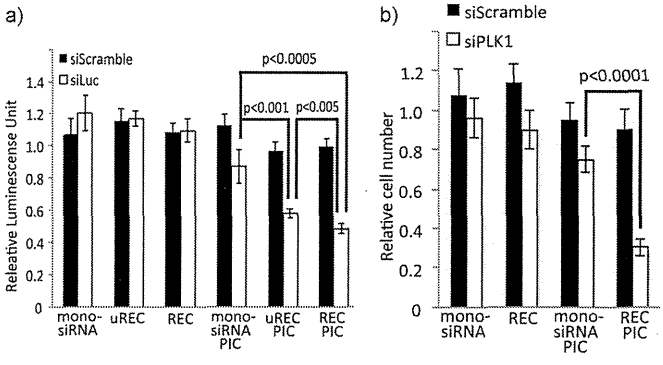

Figure 4. a) Luciferase gene expression in cultured SKOV3-Luc cells after PIC treatment at 100 nM Luc siRNA (siLuc) or scramble siRNA (siScramble) for 48 h. b) Cell viability in cultured A549 cells after PIC treatment at 100 nM PLK1 siRNA (siPLK1) or siScramble for 72 h. In both figures, results were shown as mean and standard deviation obtained from 6 samples. The *p* values were calculated according to Student's *t* test.

releasates from REC might be more readily associated with the gene silencing pathway owing to compromised steric hindrance compared to the conjugated structure. Also, no cytotoxicity was observed for all the tested PIC formulations under the same conditions as the gene-silencing assay (Supporting Information, Figure S10). Significantly stronger luciferase gene silencing of REC PICs was also confirmed in comparison with mono-siRNA PICs prepared with PAsp(DET)/PAsp(DET-CDM) (a non-covalent control) and a commercially available reagent ExGen500 (linear polyethylenimine; Supporting Information, Figure S11), demonstrating the advantage of REC formulation, including covalent conjugation between siRNA and the backbone polymer. The effect of the siRNA-releasability of REC was further examined from the standpoint of immune responses; IFNα response was determined as an indicator of immune response by enzyme-linked immunosorbent assay (ELISA). REC, uREC, and their PICs did not induce a detectable level of IFNα production for SKOV3-Luc cells ($< 10\,pg\,mL^{-1}$, data not shown). Thus, the similar ELISA experiment was further challenged for murine macrophage cells (Raw264.7), which are known to be highly sensitive to immunogen.[14] As a result, REC PICs induced a significantly lower level of IFNα production ($24.3 \pm 3.5\,pg\,mL^{-1}$) compared to uREC PICs ($60.8 \pm 12.9\,pg\,mL^{-1}$, $p < 0.005$), indicating that the siRNA-releasability based on MAA linkage successfully decreased the immune response for siRNA conjugates. Uncomplexed REC and uREC without polycation did not induce a detectable level of IFNα production, suggesting that they should not stimulate IFNα response at least on the cellular surface. Finally, the utility of REC PICs was verified for other cell lines, using a therapeutic siRNA targeting polo-like kinase 1 (PLK1). PLK1 is known to be a cell cycle regulator, and thus its silencing can arrest the cell cycle toward the apoptosis.[15] REC PICs with PLK1 siRNA (N/P 20) sequence-specifically suppressed the growth of human lung carcinoma cells (A549) and human hepatocarcinoma cells (Huh-7; Figure 4b; Supporting Information, Figure S12, respectively), demonstrating a strong potential of the REC formulation bearing the MAA linkage for siRNA-based cancer therapy.

In summary, an acidic pH-responsive siRNA conjugate was developed for enhanced siRNA delivery with reduced immunogenicity. A single chemical process based on the MAA linkage successfully provided the multifunctionality required for successful siRNA delivery; that is, reversible carrier stability, endosomal escapability, and mono-siRNA releasability. Ultimately, the siRNA conjugate sequence-specifically achieved the significant growth inhibition of cancerous cells. The programmed siRNA delivery based on the smart conjugate will be further investigated for the success in siRNA therapeutics.

Received: January 9, 2013
Revised: February 25, 2013
Published online: April 29, 2013

Keywords: conjugation · drug delivery · drug design · polymers · siRNA

[1] a) S. M. Elbashir, J. Harborth, W. Lendeckel, A. Yalcin, K. Weber, T. Tuschl, *Nature* **2001**, *411*, 494–498; b) J. C. Burnett, J. J. Rossi, *Chem. Biol.* **2012**, *19*, 60–71.

[2] R. L. Kanasty, K. A. Whitehead, A. J. Vegas, D. G. Anderson, *Mol. Ther.* **2012**, *20*, 513–524.

[3] a) D. B. Rozema, D. L. Lewis, D. H. Wakefield, S. C. Wong, J. J. Klein, P. L. Roesch, S. L. Bertin, T. W. Reppen, Q. Chu, A. V. Blokhin, J. E. Hagstrom, J. A. Wolf, *Proc. Natl. Acad. Sci. USA* **2007**, *104*, 12982–12987; b) Y. Singh, P. Murat, E. Defrancq, *Chem. Soc. Rev.* **2010**, *39*, 2054–2070; c) M. R. Alam, X. Ming, M. Fisher, J. G. Lackey, K. G. Rajeev, M. Manoharan, R. L. Juliano, *Bioconjugate Chem.* **2011**, *22*, 1673–1681; d) S. K. Lee, A. Siefert, J. Beloor, T. M. Fahmy, P. Kumar, *Methods Enzymol.* **2012**, *502*, 91–122.

[4] a) A.-L. Bolcato-Bellemin, M.-E. Bonnet, G. Creusat, P. Erbacher, J.-P. Behr, *Proc. Natl. Acad. Sci. USA* **2007**, *104*, 16050–16055; b) H. Mok, S. H. Lee, J. W. Park, T. G. Park, *Nat. Mater.* **2010**, *9*, 272–278; c) H. Takemoto, A. Ishii, K. Miyata, M. Nakanishi, M. Oba, T. Ishii, Y. Yamasaki, N. Nishiyama, K. Kataoka, *Biomaterials* **2010**, *31*, 8097–8105; d) C. A. Hong, S. H. Lee, J. S. Kim, J. W. Park, K. H. Bae, H. Mok, T. G. Park, H. Lee, *J. Am. Chem. Soc.* **2011**, *133*, 13914–13917; e) S. J. Lee, M. S. Huh, S. Y. Lee, S. Min, S. Lee, H. Koo, J. U. Chu, K. E. Lee, H. Jeon, Y. Choi, K. Choi, Y. Byun, S. Y. Jeong, K. Park, K. Kim, I. C. Kwon, *Angew. Chem.* **2012**, *124*, 7315–7319; *Angew. Chem. Int. Ed.* **2012**, *51*, 7203–7207.

[5] A. Judge, I. MacLachlan, *Hum. Gene Ther.* **2008**, *19*, 111–124.

[6] a) C. Troiber, E. Wagner, *Bioconjugate Chem.* **2011**, *22*, 1737–1752; b) J. Nguyen, F. C. Szoka, *Acc. Chem. Res.* **2012**, *45*, 1153–1162.

[7] a) D. B. Rozema, K. Ekena, D. L. Lewis, A. G. Loomis, J. A. Wolff, *Bioconjugate Chem.* **2003**, *14*, 51–57; b) S. Guo, Y. Huang, Q. Jiang, Y. Sun, L. Deng, Z. Liang, Q. Du, J. Xing, Y. Zhao, P. C. Wang, A. Dong, X.-J. Liang, *ACS Nano* **2010**, *4*, 5505–5511.

[8] Y. Lee, K. Miyata, M. Oba, T. Ishii, S. Fukushima, M. Han, H. Koyama, N. Nishiyama, K. Kataoka, *Angew. Chem.* **2008**, *120*, 5241–5244; *Angew. Chem. Int. Ed.* **2008**, *47*, 5163–5166.

[9] K. Miyata, M. Oba, M. Nakanishi, S. Fukushima, Y. Yamasaki, H. Koyama, N. Nishiyama, K. Kataoka, *J. Am. Chem. Soc.* **2008**, *130*, 16287–16294.

[10] H. Takemoto, K. Miyata, T. Ishii, S. Hattori, S. Osawa, N. Nishiyama, K. Kataoka, *Bioconjugate Chem.* **2012**, *23*, 1503–1506.

[11] J. DeRouchey, C. Schmidt, G. F. Walker, C. Koch, C. Plank, E. Wagner, J. O. Radler, *Biomacromolecules* **2008**, *9*, 724–732.

[12] a) M. J. Palte, R. T. Raines, *J. Am. Chem. Soc.* **2012**, *134*, 6218–6223; b) M. Zheng, D. Librizzi, A. Kılıç, Y. Liu, H. Renz, O. M. Merkel, T. Kissel, *Biomaterials* **2012**, *33*, 6551–6558.

[13] K. Whitehead, G. Sahay, G. Z. Li, K. T. Love, C. A. Alabi, M. Ma, C. Zurenko, W. Querbes, R. S. Langer, D. G. Anderson, *Mol. Ther.* **2011**, *19*, 1688–1694.

[14] J. Turco, H. H. Winker, *Infect. Immun.* **1982**, *35*, 783–791.

[15] a) A. D. Judge, M. Robbins, I. Tavakoli, J. Levi, L. Hu, A. Fronda, E. Ambegia, K. McClintock, I. MacLachlan, *J. Clin. Invest.* **2009**, *119*, 661–673; b) K. Strebhardt, *Nat. Rev. Drug Discovery* **2010**, *9*, 643–660.

Bioorganic & Medicinal Chemistry 21 (2013) 1717–1723

Contents lists available at SciVerse ScienceDirect

Bioorganic & Medicinal Chemistry

journal homepage: www.elsevier.com/locate/bmc

Synthesis and properties of cationic oligopeptides with different side chain lengths that bind to RNA duplexes

Yusuke Maeda, Rintaro Iwata, Takeshi Wada *

Department of Medical Genome Sciences, Graduate School of Frontier Sciences, The University of Tokyo, Bioscience Building 702, Kashiwanoha, Kashiwa, Chiba 277-8562, Japan

ARTICLE INFO

Article history:
Received 4 January 2013
Revised 22 January 2013
Accepted 23 January 2013
Available online 1 February 2013

Keywords:
RNA-binding peptide
Cationic peptide
Artificial peptide
RNAi drug
DDS

ABSTRACT

A series of artificial peptides bearing cationic functional groups with different side chain lengths were designed, and their ability to increase the thermal stability of nucleic acid duplexes was investigated. The peptides with amino groups selectively increased the stability of RNA/RNA duplexes, and a relationship between the side chain length and the melting temperature (T_m) of the peptide–RNA complexes was observed. On the other hand, while peptides with guanidino groups exhibited a similar tendency with respect to the peptide structure and thermal stability of RNA/RNA duplexes, those with longer side chain lengths, such as L-2-amino-4-guanidinobutyric acid (Agb) or L-arginine (Arg) oligomers, stabilized both RNA/RNA and DNA/DNA duplexes, and those with shorter side chain lengths exhibited a higher ability to selectively stabilize RNA/RNA duplexes. In addition, peptides were designed with different levels of flexibility by introducing glycine (Gly) residues into the L-2-amino-3-guanidinopropionic acid (Agp) oligomers. It was found that insertion of Gly did not affect the thermal stability of the peptide–RNA complexes, but an alternate arrangement of Gly and Agp apparently decreased the thermal stability. Therefore, in the Agp oligomer, consecutive Agp sequences are essential for increasing the stability of RNA/RNA duplexes.

1. Introduction

In recent years, increased attention has been paid to the development of nucleic acid drugs. For example, antisense oligonucleotides and RNA interference drugs (RNAi drugs) are well known molecular tools for the regulation of gene expression, in which their mechanisms of action are based on sequence specific interactions.[1] The RNAi drugs act on the target mRNA in a sequence selective manner. Thus, RNAi drugs are attractive because of their high selectivity for the target and their shorter drug development time. Therefore, siRNAs have been widely studied for therapeutic applications; however, such RNA molecules are not sufficiently effective because of their low-membrane permeability and instability in cells. To stabilize oligonucleotides against metabolic degradation, a number of chemical modifications have been proposed,[2] and RNAi drugs generally consist of double stranded RNAs (dsRNAs) with chemical modifications. A proper modification of an RNA molecule increases its stability in cells and improves its pharmacokinetic properties.[3] Another strategy for stabilizing siRNA is the use of molecules that can non-covalently bind to RNA to protect it from attack by nucleases. For example, a fusion protein of the peptide transduction domain-dsRNA binding domain was shown to effectively transport RNAi drugs into primary cells.[4] In this case, the increased thermal stability of the dsRNAs also increased their stability in cells.[5] We are thus attempting to develop RNA/RNA duplex-binding molecules that are useful as drug delivery systems (DDSs) for siRNAs.

A wide variety of RNA-binding molecules have been reported, such as aminoglycosides[6] and RNA-binding proteins.[7] In paticular, chemically modified peptides bearing different methylene lengths in the arginine or lysine residues possess diverse affinities to RNAs.[8] In our previous study, α-(1 → 4)-linked-2,6-diamino-2,6-dideoxy-D-glucopyranose oligomers were synthesized, and their highly RNA-selective binding ability was demonstrated.[9] These results suggested that the geometry of the cationic groups, particularly the distance between the cationic groups, affects the affinity and selectivity of the oligomers for nucleic acid duplexes. Therefore, in this study, we designed a series of cationic oligopeptides to reveal the relationship between the geometry of the cationic groups and the affinity of the peptides for nucleic acids. In contrast to oligosaccharide derivatives, peptides can easily be synthesized, which is advantageous for obtaining a systematic series of molecules. They can also be readily connected with other functional groups such as transporter molecules.[10] Therefore, RNA duplex-binding peptides are useful tools for the development of drug delivery systems (DDSs) for RNAi drugs. The L-arginine (Arg) oligomers designed from the HIV Tat peptide are well known for their high-membrane permeability[11] and the Arg 15mer has been used as an RNAi transporter by forming a complex with RNA.[12]

* Corresponding author. Tel.: +81 4 7136 3611.
E-mail address: wada@k.u-tokyo.ac.jp (T. Wada).

0968-0896/$ - see front matter © 2013 Elsevier Ltd. All rights reserved.
http://dx.doi.org/10.1016/j.bmc.2013.01.053

However, the activity varies with the side chain length,[13] and thus a more detailed study of the relationship between the structure and activity is important for the development of effective carriers for RNAi drugs. Thus, to investigate the structural effects on binding ability, we designed and synthesized a number of cationic oligopeptides bearing different side chain lengths to control the distance between the cationic functional groups and peptides with different flexibility by incorporating glycine (Gly).

2. Results and discussion

2.1. Design of the peptides

A series of cationic oligopeptides was designed (Fig. 1). All peptides contained a unit of *N*-acetyl-L-tyrosine with two glycine residues at the N-terminus for UV detection and quantification. In this study, the 12mer of nucleic acid duplexes was used as a model to estimate the interaction with peptides bearing four or eight cationic groups because four pairs of phosphate groups are aligned on the inward portion of the major groove of the 12mer of A-type nucleic acid duplexes. First, to compare the effects of the distance between cationic groups, peptides with different side chain lengths were designed. Peptides were synthesized with amino groups (L-2,3-diaminopropionic acid (Dap), L-2,4-diaminobutyric acid (Dab), L-ornithine (Orn), and L-lysine (Lys)) and guanidino groups (L-2-amino-3-guanidinopropionic acid (Agp), L-2-amino-4-guanidinobutyric acid (Agb), and L-arginine (Arg)). In some molecules, several glycine units were also inserted into an Agp octamer to increase the flexibility of the peptides. Peptides with alternate arrangements were also designed to change the position and combination of the functional groups. These peptides were based on the Agp oligomer and other amino acids such as glycine (Gly), L-serine (Ser), and L-asparagine (Asn). Glycine was chosen because of its high flexibility. Ser and Asn were chosen because they are well known in RNA-binding proteins to form hydrogen bonds with the phosphate groups of RNA.[14]

On the basis of molecular mechanics calculations with a GB/SA water solvation model,[15] a cationic oligopeptide 8mer consisting of Dab can bind to the major groove of an A-type RNA/RNA duplex 12mer, in which all the protonated amino groups of the peptide form the hydrogen bonds to the phosphate anions of the duplex (Fig. 2). Therefore, the electrostatic interaction and hydrogen bonding would be important for the binding of cationic oligopeptides to RNA/RNA duplexes.

2.2. Melting temperature (T_m) analysis

The T_m values of the RNA duplexes were measured both in the absence and presence of an equal amount of peptides. All measurements were performed under-physiological conditions with 10 mM phosphate buffer containing 100 mM NaCl at pH 7.0. Figure 2 shows the melting temperature enhancements and Table 1 lists the T_m values for the self complementary RNA 12mer r(CGCGAAUUCGCG)$_2$ in the absence and presence of an equal amount of peptides with amino groups. In this study, the peptides were added into the solution of nucleic acid duplexes after annealing to avoid the aggregation of the peptides at high temperature. The T_m values were affected by the side chain length, with Dab_8 (**2**) showing the highest T_m value. Comparing the Dab_8 (**2**), Orn_8 (**3**), and Lys_8 (**4**), the T_m value increased as the side chain length

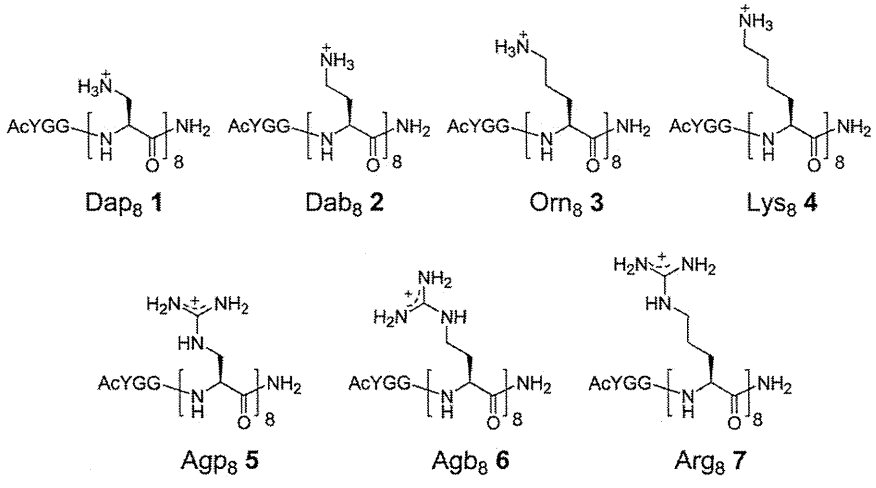

Peptides with amino groups		**Peptides with flexible main chains**	
Dap_8 : Ac-YGG-Dap_8-NH_2 **1**		Agp_8G1 : Ac-YGG-Agp_4-G-Agp_4-NH_2	**8**
Dab_8 : Ac-YGG-Dab_8-NH_2 **2**		Agp_8G2 : Ac-YGG-Agp_3-G-Agp_2-G-Agp_3-NH_2	**9**
Orn_8 : Ac-YGG-Orn_8-NH_2 **3**		Agp_8G3 : Ac-YGG-Agp_2-G-Agp_2-G-Agp_2-G-Agp_2-NH_2	**10**
Lys_8 : Ac-YGG-Lys_8-NH_2 **4**		Agp_8A2 : Ac-YGG-Agp_3-A-Agp_2-A-Agp_3-NH_2	**11**
Peptides with guanidino groups		Agp_8P2 : Ac-YGG-Agp_3-P-Agp_2-P-Agp_3-NH_2	**12**
Agp_8 : Ac-YGG-Agp_8-NH_2 **5**		**Peptides with alternate arrangement**	
Agb_8 : Ac-YGG-Agb_8-NH_2 **6**		AgpG : Ac-YGG-$(Agp\text{-}G)_4$-NH_2	**13**
Arg_8 : Ac-YGG-Arg_8-NH_2 **7**		AgpS : Ac-YGG-$(Agp\text{-}S)_4$-NH_2	**14**
		AgpN : Ac-YGG-$(Agp\text{-}N)_4$-NH_2	**15**

Figure 1. Structures and sequences of cationic peptides.

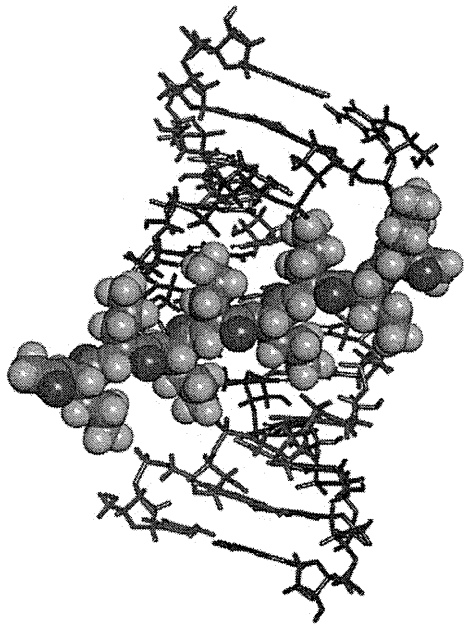

Figure 2. Molecular model of L-2,4-diaminobutylic acid (Dab) 8mer binding to A-type RNA–RNA duplex (12mer).

Table 1
Thermal melting points (T_m in °C) for oligonucleotide duplex (in the absence and presence of peptides with amino groups[a])[b]

Peptide	RNA/RNA	ΔT_m	DNA/DNA	ΔT_m
None	60.7		48.2	
Dap_8	60.2	−0.5	50.8	2.6
Dab_8	74.7	14.0	49.5	1.3
Orn_8	74.2	13.5	51.3	3.1
Lys_8	68.1	7.4	49.7	1.5

[a] Peptide concentration 4 μM.
[b] Buffer (10 mM phosphate buffere for pH 7.0), NaCl (100 mM), together with each oligonucleotide strand (4 μM). T_m values are reported at the means of duplicate measurements.

decreased. These results suggest that the distance between the amino groups in Dab_8 (**2**) fits to the distance of the opposing phosphate groups in the RNA duplexes. This tendency has been previously reported for cationic oligopeptides with D-amino acids.[6] On the other hand, Dap_8 (**1**) did not stabilize the RNA/RNA duplexes. This differing behavior may result because the distance of the amino groups in Dap_8 is too short to interact with the phosphate groups in the RNA/RNA duplexes. In fact, none of the peptides with amino groups increased the thermal stability of the DNA/DNA duplex d(CGCGAATTCGCG)$_2$ (Fig. 3). The distance between the phosphate groups in the major groove of a DNA/DNA duplex is twice that in an RNA/RNA duplex. Therefore, none of the peptides were able to interact with the DNA/DNA duplexes. In the minor groove of a DNA/DNA duplex, the interstrand phosphate groups are much closer than those in the major groove. However, the phosphate groups facing outward of the minor groove are unfavorable to form hydrogen bonds with the protonated amino groups of cationic peptides.

The peptides with guanidino groups (**5**, **6**, **7**) exhibited the same tendency as the peptides with the amino groups (Fig. 4, Table 2) for the RNA/RNA duplexes. Peptides with shorter side chain lengths had higher T_m values. This result indicates that the position of guanidino groups in Agp_8 (**5**) also fits well with the RNA duplex structure. While the distance between the functional groups is similar in the peptides with amino and guanidino groups, the peptides with

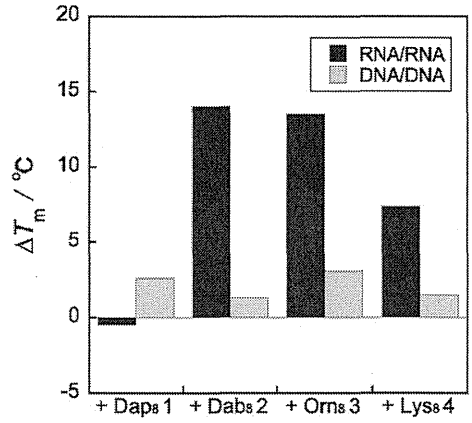

Figure 3. Melting temperature enhancements for the RNA/RNA and DNA/DNA duplexes at pH 7.0 in the presence of peptides **1–4**. Differences in the thermal melting points (ΔT_m) are given for the nucleic acid duplexes in the presence of equimolar amounts of peptide relative to the duplex alone. The dark gray columns represent ΔT_m for RNA/RNA duplex, and light gray columns represent ΔT_m values for DNA/DNA duplex.

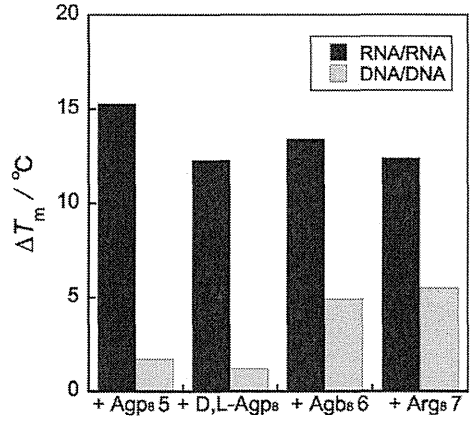

Figure 4. Melting temperature enhancements for the RNA/RNA and DNA/DNA duplexes at pH 7.0 in the presence of peptides **5–7**. Differences in the thermal melting points (ΔT_m) are given for the nucleic acid duplexes in the presence of an equal amount of peptide relative to the duplex alone. The dark gray columns represent ΔT_m for RNA/RNA duplex, and light gray columns represent ΔT_m values for DNA/DNA duplex.

Table 2
Thermal melting points (T_m in °C) for oligonucleotide duplex (in the absence and presence of peptides with guanidino groups[a])[b]

Peptide	RNA/RNA	ΔT_m	DNA/DNA	ΔT_m
None	60.7		48.2	
Agp_8	76.9	16.2	49.9	1.7
D-Agp_8	75.8	15.1	48.9	0.7
D,L-Agp_8	73.0	12.3	49.4	1.2
Agb_8	74.1	13.4	53.1	4.9
Arg_8	73.1	12.4	53.7	5.5

[a] Peptide concentration 4 μM.
[b] Buffer (10 mM phosphate buffere for pH 7.0), NaCl (100 mM), together with each oligonucleotide strand (4 μM). T_m values are reported at the means of duplicate measurements.

the guanidino groups exhibited higher T_m values. These different T_m values can be attributed to the different features of the functional groups. The guanidino group is known to have a stronger interaction with phosphate groups than amino groups, and thus the peptides with guanidino groups showed a stronger interaction

with the nucleic acid duplexes. However, in the case of the DNA/DNA duplex, the tendency changed because of the differences in the guanidino and amino functional groups. For the peptides with guanidine groups, those with longer side chain lengths had higher T_m values. This result may also be due to the fact that the guanidino groups strongly interact with the phosphate groups.

The different side chain lengths of the peptides resulted in different thermal stabilities of the nucleic acid duplexes. The duplex stability may also be affected by the flexibility of the peptides. Thus, to investigate the effect of incorporation of flexible residues into the peptide backbone, glycine was inserted into Agp_8 (**5**) to increase the flexibility of the main chain (**8**, **9**, **10**). Interestingly, it was found that an increase in the flexibility of the main chain did not affect the thermal stability of the peptide–RNA complexes (Fig. 5, Table 3). These results suggest that the stabilization of the RNA duplex with Agp_8 (**5**) is mainly attributed to enthalpic factors. In addition, insertion of L-alanine (Ala) or L-proline (Pro) into Agp_8 (**5**) also did not affect the thermal stability of the RNA duplexes (**11**, **12**). If the peptides invade the major groove, the redundant amino acid residues will give rise to steric hindrance and decrease the thermal stability. Therefore, these results suggest that the peptides interact with the surface of the nucleic acids.

Peptides with alternate arrangements also did not stabilize the RNA duplexes (Fig. 6, Table 4). Peptides consisting of Agp and Gly in an alternate arrangement, AgpG (**13**) did not have any effects on the RNA/RNA duplex. On the other hand, Agp_4 showed an appreciable stabilization effect for the RNA/RNA duplex. Therefore, a consecutive Agp sequence is effective for RNA/RNA duplex stabilization. Furthermore, Agp_8G3 (**10**), in which four Agp_2 units are connected, has the same affinity as Agp_8; thus, the Agp_2 structural unit is effective for the interaction with RNA/RNA duplexes. In Agp oligomers with a consecutive sequence, the guanidino groups are located on both sides of the peptide backbone, and this alignment is identical to that required for interaction between the guanidino groups and the phosphates in the major groove of RNA duplexes. However, peptides with a combination of guanidino and hydroxy or amide groups (AgpS (**14**) and AgpN (**15**), respectively) had no effects on the thermal stability of RNA duplexes. These results also suggest that a consecutive arrangement of cationic amino acids is essential for effective interaction with the phosphates of RNA duplexes.

The effect of chirality was also examined. The Agp oligomers consisting of all-L- and all-D-amino acids had similar T_m values,

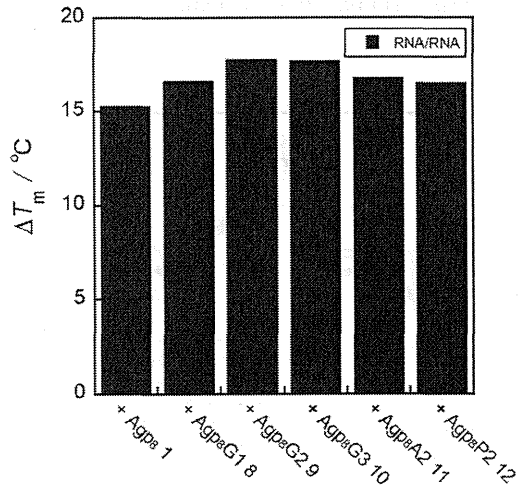

Figure 5. Melting temperature enhancements for the RNA/RNA duplexes at pH 7.0 in the presence of peptides **1**, **8**–**12**. Differences in the thermal melting points (ΔT_m) are given for the nucleic acid duplexes in the presence of an equal amount of peptide relative to the duplex alone.

Table 3
Thermal melting points (T_m in °C) for oligonucleotide duplex (in the absence and presence of peptides with flexible main chian[a])[b]

Peptide	RNA/RNA	ΔT_m
None	60.9	
Agp_8	77.5	16.6
Agp_8G1	77.5	16.6
Agp_8G2	78.8	17.9
Agp_8G3	78.6	17.7
Agp_8A2	77.7	16.8
Agp_8P2	77.4	16.5

[a] Peptide concentration 4 μM.
[b] Buffer (10 mM phosphate buffere for pH 7.0), NaCl (100 mM), together with each oligonucleotide strand (4 μM). T_m values are reported at the means of duplicate measurements.

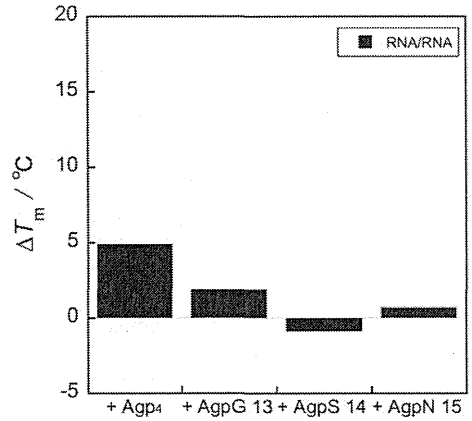

Figure 6. Melting temperature enhancements for the RNA/RNA duplexes at pH 7.0 in the presence of peptides **13**–**15**. Differences in the thermal melting points (ΔT_m) are given for the nucleic acid duplexes in the presence of equimolar amounts of peptide relative to the duplex alone.

Table 4
Thermal melting points (T_m in °C) for oligonucleotide duplex (in the absence and presence of peptides with alternate arrangements[a])[b]

Peptide	RNA/RNA	ΔT_m
None	60.3	
Agp_4	65.2	4.9
AgpG	62.2	1.9
AgpS	58.9	−1.4
AgpN	60.5	0.2

[a] Peptide concentration 4 μM.
[b] Buffer (10 mM phosphate buffere for pH 7.0), NaCl (100 mM), together with each oligonucleotide strand (4 μM). T_m values are reported at the means of duplicate measurements.

but the peptides having D/L-alternate arrangements slightly had lower thermal stability. A decrease in the thermal stability induced by a heterochiral backbone was also reported for chiral PNA.[16]

2.3. CD spectroscopy

The structures of the peptides and the RNA–peptide complexes in solution were analyzed using circular dichroism (CD) spectroscopy. On the basis of molecular mechanics calculations,[15] the amino groups and guanidino groups of the peptides, particularly in Dap_8 (**2**) and Agp_8 (**5**), can form intramolecular hydrogen bonds with the amido groups in the main chain. However, in the absence of nucleic acid duplexes, the spectra of all the peptides indicated the presence of random coils.[17] Therefore, the effect of the secondary structures of the peptides was negligible in these cases. The

structures of the RNA–peptide complexes were also analyzed. Because the peptides showed a variety of T_m values depending on the side chain length and the nature of the cationic functional groups, there existed not only electrostatic interactions and hydrogen bonding, but also structural factors. However, for both the RNA and DNA duplexes, no appreciable structural changes in the nucleic acids were observed following the addition of the peptides (Figs. 7 and 8). The CD spectra of the RNA and DNA duplexes in the presence and absence of peptides were typical for A-type and B-type helices, respectively.

2.4. ITC measurement

Thermodynamic analysis of the peptide–nucleic acid interactions was carried out using isothermal titration calorimetry (ITC) measurements. The duplex concentration was 2.5 times higher than that used for the UV melting analyses because the amount of heat generated during the binding between the nucleic acid duplexes and the oligocationic peptides was expected to be insufficient for calculation of the thermodynamic parameters at the lower concentration. Figures 9, S8,[17] and S9[17] show the preliminary results for the ITC titration of the peptides with the self complementary RNA/RNA duplex r(CGCGAAUUCGCG)$_2$ and DNA/DNA duplex d(CGCGAATTCGCG)$_2$. In addition to electrostatic interactions and hydrogen bonding between the peptides and nucleic acids, dehydration and dissociation of the phosphates in the buffer solution were apparently observed. Thus, the interactions were too complex for calculation of the thermodynamical parameters. However, it was observed that both of the peptides selectively interacted with the RNA/RNA duplexes. In contrast, only Agb$_8$ (**5**) interacted with both the RNA/RNA and DNA/DNA duplexes. This result may be due to the fact that, in Agb$_8$, the side chain is long and sufficiently flexible to interact with the phosphate groups of both the RNA/RNA and DNA/DNA duplexes. In comparison with the amino-substituted Dap$_8$, the guanidine-substituted Dab$_8$ (**5**) had larger endothermic interactions.

Inhibition assays were carried out to clarify the peptide-binding sites in the RNA duplexes. The peptides were titrated into a solution of the RNA duplexes in the presence of neomycin, which is known to bind to the major groove of RNA duplexes.[18] The inhibition of peptide–RNA binding by neomycin was different for the types of peptides (Fig. S10[17]). For Dab$_8$ (**2**), the exothermic interactions were selectively inhibited, while the endothermic interactions were still observed. On the other hand, for Agp$_8$ (**5**), both of the interactions were inhibited. These results suggest that the exothermic interactions are attributed to the binding of the peptides to the major groove of RNA/RNA duplexes and the endothermic interactions are related to the interactions with other sites.

3. Materials and methods

3.1. Peptide synthesis

Peptides were synthesized via a conventional solid-phase method by using the 9-fluorenylmethyloxycarbonyl (Fmoc) strategy.[19] The peptide chains were assembled on a Fmoc-NH-SAL-PEG resin by using Fmoc amino acid derivatives (5 equiv), *N,N*-diisopropylethylamine (DIPEA, 10 equiv), and 2-(1*H*-9-azabenzotriazole-1-yl)-1,1,3,3-tetramethyluronium hexafluorophosphate (HATU, 5 equiv) in dimethylformamide (DMF) for the coupling, and 25% piperidine/DMF for the removal of the Fmoc group. After coupling of the last amino acids, amino groups at the N-termini were protected with an acetyl (Ac) group using acetic anhydride (10 equiv). To cleave the peptide from the resin and remove the side chain protecting groups, the peptide resin was treated with trifluoroacetic acid (TFA)-triisopropylsilane-water, (95:2.5:2.5, v/v/v). Peptides in sat $NaHCO_{3aq}$ (200 μl) were added in one portion to a solution of the 1,3-di-Boc-2-(trifluoromethylsulfonyl)guanidine[20] (10 equiv per amino groups) in dioxane (200 μl), and stirred overnight at rt, then concentrated in vacuo. To remove the protecting groups from the guanidino groups, the peptides were treated with TFA–triisopropylsilane–water (95:2.5:2.5, v/v/v). All peptides were purified with reverse-phase HPLC (0.05% TFA in water–acetonitrile). The peptides were successfully identified by matrix-assisted laser desorption ionization time-of-flight mass spectrometry (MALDI-TOF-MS). Compound **1**, TOF-MS *m/z* calcd for $[M+Na]^+$ 1048.07; Found 1047.60. Compound **2**, TOF-MS *m/z* calcd for $[M+H]^+$ 1138.31; Found 1137.22. Compound **3**, TOF-MS *m/z* calcd for $[M+Na]^+$ 1272.50; Found 1271.56. Compound **4**, TOF-MS *m/z* calcd for $[M+H]^+$ 1362.73; Found 1361.51. Compound **5**, TOF-MS *m/z* calcd for $[M+H]^+$ 1362.41; Found 1361.51. Compound **6**, TOF-MS *m/z* calcd for $[M+H]^+$ 1474.63; Found 1473.77. Compound **7**, TOF-MS *m/z* calcd for $[M+H]^+$ 1586.84; Found 1585.72. Compound **8**, TOF-MS *m/z* calcd for $[M+H]^+$ 1419.46; Found 1418.53. Compound **9**, TOF-MS *m/z* calcd for $[M+Na]^+$ 1476.52; Found 1476.00. Compound **10**, TOF-MS *m/z* calcd for $[M+H]^+$ 1533.57; Found 1533.07. Compound **11**, TOF-MS *m/z* calcd for $[M+H]^+$ 1504.57; Found 1504.21. Compound **12**, TOF-MS *m/z* calcd for $[M+H]^+$ 1556.64; Found 1555.68. Compound **13**, TOF-MS *m/z* calcd for $[M+Na]^+$ 1100.07; Found 1099.25. Compound **14**, TOF-MS *m/z*

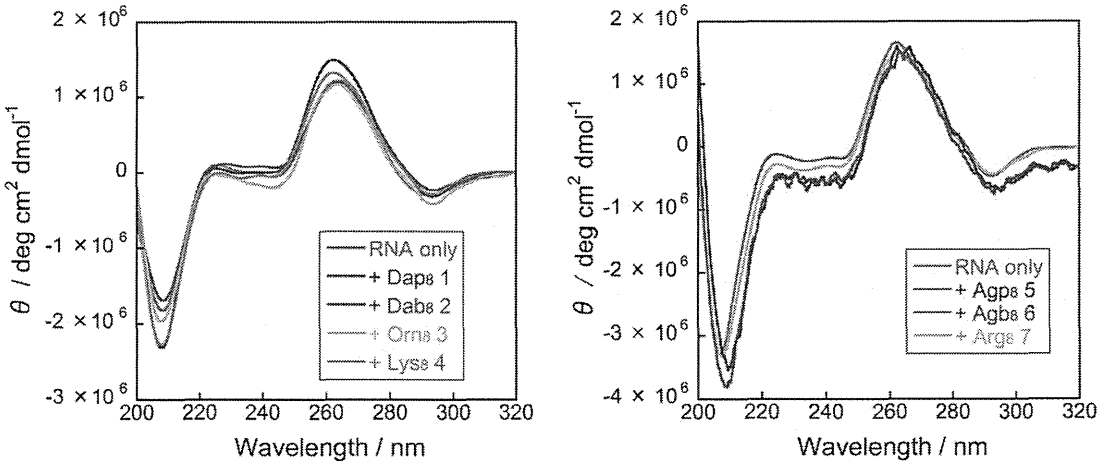

Figure 7. CD spectra of the RNA/RNA duplexes in the presence and absence of an equal amount of peptides **1–7** (at 20 °C, pH 7.0, 4 μM each of peptide and duplex).